POLITECNICO
MILANO 1863

SCUOLA DI INGEGNERIA INDUSTRIALE E DELL'INFORMAZIONE

Synthesis and Structural Design of Co, Ni-free Disorder Rock-Salt Cathode Materials for Lithium-ion Batteries Via Novel Mechanochemical Ball Milling Method

TESI DI LAUREA MAGISTRALE IN
ENERGY ENGINEERING-INGEGNERIA ENERGETICA

Author: **Abdulrahman Hamdy Abdulrasoul Mahgoub Hassan Elsharkawy**

Student ID:	10771090
Advisor:	Professor Jie Li
Academic Year:	2022-2023

I. ABSTRACT

Li-excess cation disordered rocksalt (DRX) cathodes have gained significant attention in the field of Li-ion batteries due to their high capacities and the utilization of abundant transition metals. In this study, a novel technique employing dry ball milling is introduced as a simple, low cost, and energy-efficient method for synthesizing DRX cathodes. Additionally, cation deficiency engineering is explored to optimize the overall electrochemical performance of the DRX cathodes, as cation vacancy is expected to improve Li percolation and provides additional sites for Li ions intercalation, thereby increasing the specific capacity of the materials. The proof-of-concept material, $Li_{1.25}Fe_{0.5}Nb_{0.25}O_2$/C, is used to demonstrate the effectiveness of the new synthesis technique. It is observed that the desired DRX phase can be achieved via dry milling approach, however, often with impure phases leading to reduced capacity and fast capacity fade. Furthermore, even though the introduction of 2% and 6% cation vacancies through dry milling shows cation advantageous, it should be noted that introducing cation vacancies through that technique, particularly at higher vacancy levels, can also lead to structural instability and poor cycling stability. This instability may result in material degradation, capacity loss, and diminished battery performance. Thus, dry ball milling is an interesting technique for synthesis of DRX cathodes, but the systematic optimization, regarding the milling speed and duration, the weight ratio of material and balls, is necessary for each target material.

II. ABSTRACT ITALIANO

I catodi Li-excess cation disordered rocksalt (DRX) hanno attirato molta attenzione nel campo delle batterie al litio grazie alla loro elevata capacità e all'utilizzo di metalli di transizione presenti in maniera abbondante sul pianeta Terra. In questo studio viene presentata una nuova tecnica che utilizza la frantumazione a secco mediante mulino a sfere (ball milling) come metodo non complesso , economico ed energeticamente efficiente per la sintesi di catodi DRX. Inoltre, viene esaminata l'ingegnerizzazione dei catodi Li-excess cation disordered rocksalt (DRX) per ottimizzare le prestazioni elettrochimiche complessive dei catodi DRX, poiché si prevede che un maggior numero di posti vacanti nella struttura cristallina del materiale migliori la percolazione del litio e fornisca siti aggiuntivi per l'intercalazione degli ioni di litio, aumentando così la capacità specifica dei materiali. Il materiale di prova, $Li_{1.25}Fe_{0.5}Nb_{0.25}O_2$/C, viene utilizzato per dimostrare l'efficacia della nuova tecnica di sintesi. Si osserva che la fase DRX desiderata può essere ottenuta mediante l'approccio di frantumazione a secco, tuttavia spesso con fasi impure che portano a una capacità ridotta e a un rapido decadimento della capacità. L'introduzione di vuoti nella struttura cristallina del 2% e del 6% tramite il metodo oggetto della ricerca mostra alcuni vantaggi, tuttavia può anche portare a un'instabilità strutturale del materiale che si riflette in una scarsa stabilità durante i cicli di carica/scarica con conseguente degrado del materiale, perdita di capacità e riduzione delle prestazioni della batteria. Pertanto, la frantumazione a secco mediante mulino a sfere è una tecnica interessante per la sintesi di catodi DRX, ma è necessaria un'ottimizzazione sistematica, riguardo alla velocità e alla durata della frantumazione, al rapporto di peso tra materiale e sfere, per ogni materiale target, in questo modo sarà possibile ridurre la presenza di fasi impure e limitare il decadimento delle proprietà strutturali e elettrochimiche del materiale.
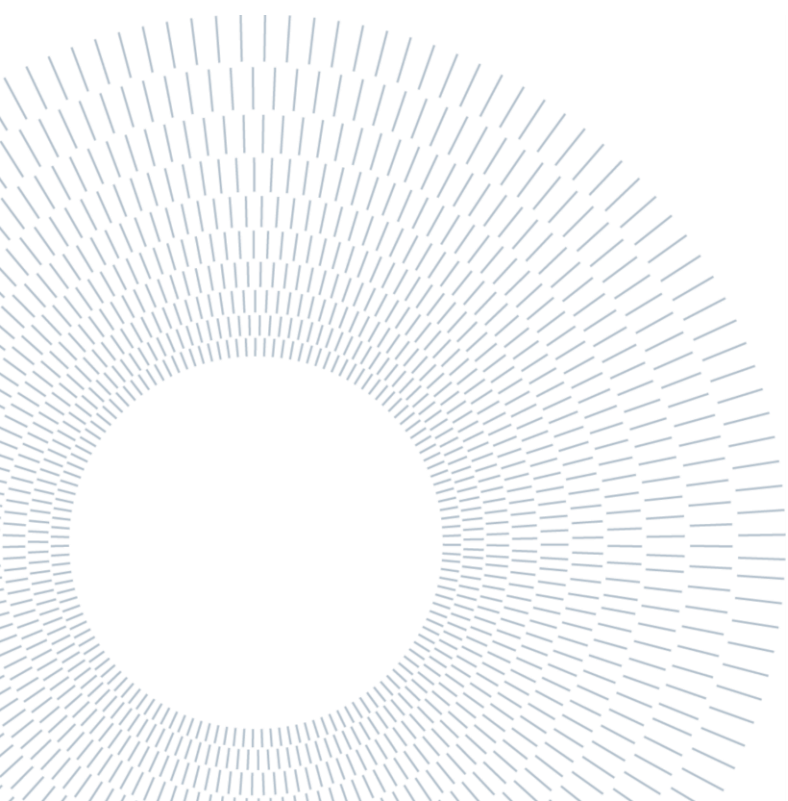
TABLE OF CONTENTS

LIST OF FIGURES

LIST OF TABLES

III. INTRODUCTION

III-1 Lithium-ion batteries

Rechargeable batteries with increased capacity or smaller size and weight for a given capacity became increasingly necessary throughout the 1980s due to the growth of portable electronic goods such as video cameras, notebook computers, and mobile phones[1]. In general, batteries work to transform chemical energy that has been stored into electricity. Two electrodes, the cathode and the anode, are where electrochemical conversion occurs. The chemistry of the electrodes determines the type of reaction. While the energy content is more dependent on the mass and volume of the active material, the power of the battery is more directly influenced by the area of the electrodes [4]. The well applied secondary battery systems include lead-acid batteries, nickel-cadmium batteries, nickel-metal hydride batteries, and lithium-ion batteries (LIBs) etc. Among them, the technology for lead-acid batteries has been around for more than a century and has a strong track record. However, it has low volumetric and gravimetric energy densities. Batteries made of nickel metal hydride are frequently seen in hybrid cars because they offer stable cyclability. Their disadvantages include a relatively low energy density, short cycle life, and a high self-discharge rate of up to 10% monthly. In one word, the size and weight of those conventional rechargeable batteries face restrictions for the application in the modern society. Thus, in order to satisfy the growing demand for power supply for portable electronics, lithium-ion batteries (LIBs) have been significantly developed since it was first conceptualized in the early 1980s [1,3]. For these types of rechargeable batteries, the volumetric and gravimetric energy densities are shown in Figure 1 compares the volumetric and gravimetric energy densities of these battery systems.

Among different conventional battery systems, compared to lead acid or nickel-metal hydride cells, the batteries with lithium chemistry offer a cell structure that runs at a voltage that is more than twice as high. Obviously, in so called Li-metal batteries (LMBs), Li metal is a promising anode material as it has extremely high theoretical specific capacities (3860 mAh g^{-1}) and the lowest negative electrochemical potential

(−3.04 V vs. the standard hydrogen electrode). However, it has been suffering from dendritic problems, interfacial side reactions, volume change and low Coulombic efficiency, which strictly limit application of LMBs. Thus, LIBs with intercalated electrode materials, on the other hand, offer substantially superior power density and cycle life, which are being taken into consideration for usage in bigger applications like cars [6].
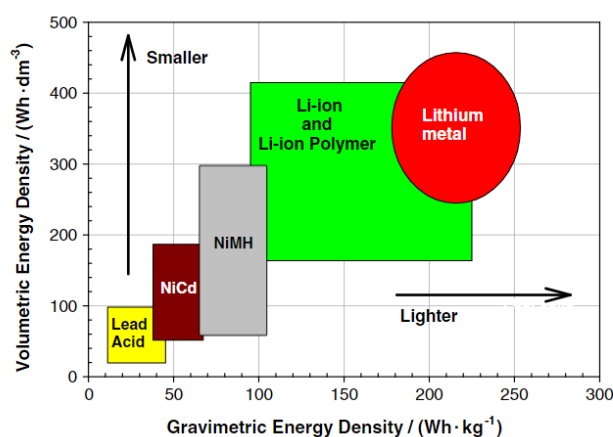
Figure 1 Plot of volumetric energy density against gravimetric energy density for common batteries [5].

In a lithium-ion battery, lithium ions are extracted from and inserted into the two electrodes in a process that is both reversible and involves the simultaneous removal and addition of electrons, if a power supply is used instead of the external load, the direction of the lithium ions and electrons is reversed, and the battery is charged. Figure 2 shows the basic working principles for a LIB. During discharge, lithium ions exit from the anode and transport to the cathode, and during charge, they move via the opposite way. Electrons migrate in the same direction as Li-ions in the external circuit. In its most conventional structure, graphite (or lithium titanate) is used as the anode (negative electrode) and lithium metal oxide is used as the cathode (positive electrode) [7].
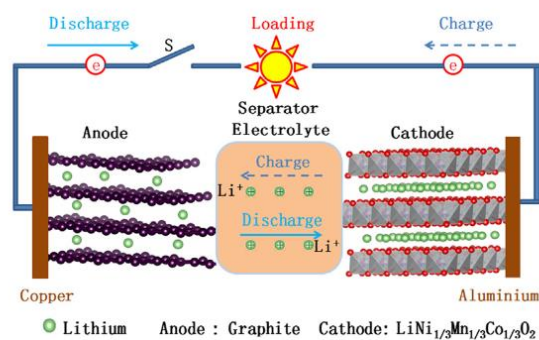
Figure 2 Schematic representation of a typical lithium-ion battery [8].

It is difficult to scale up the chemistry of conventional lithium-ion batteries for use in electronic vehicles (EVs) or renewable energy plants (REPs). This crucial step is still being prevented by many obstacles, including material availability, cost, wide temperature operating range, cycle life, and safety etc. On the other hand, the inherent advantages of lithium technology and its use in these important emerging industries have encouraged global efforts to address these issues in order to establish the lithium-ion batteries as the industry leader in both EV and REP sectors [9]. The objective is to develop the technology of lithium-ion batteries, which is directly influenced by the characteristics of the components used to make them, by replacing the present battery components with materials characterized by higher performance in terms of energy, power, cost, reliability, lifetime, and safety [10].

III-2 Challenges on cathode materials

Cathode materials, out of all the components, are the barrier to higher energy densities, hence higher performance in LIBs, because of their considerably lower specific capacities (compared to conventional anode material graphite). Therefore, the best strategy for further improving the energy density of LIBs is the development of high capacity or high working potential cathode materials [11]. Many different types of compounds have been developed as cathode materials for LIBs, such as layered oxides, spinel oxide and polyanionic compounds. Among them, Ni, Co, and Mn-based (NCM, $LiNi_xCo_yMn_zO_2$ (x+y+z=1)) layered transition metal oxide positive electrode materials have demonstrated in recent years a great potential for high-energy density LIBs, and these NCM-based batteries have successfully entered the market. Three mixed transition metal oxides, Ni, Co, and Mn, were selected because they can, respectively, enhance capacity, charge-discharge kinetics, and structural stability [12]. The design of NCM layered materials follows the phase diagram of the ternary system between $LiNiO_2$ (LNO), $LiCoO_2$ (LCO) and $LiMnO_2$ (LMO), as shown in Figure 3. Studies of NCM materials [13,14,15] with diverse Ni, Co, and Mn contents show that Ni-rich materials make excellent candidates for high-capacity batteries. Nevertheless, very much like $LiNiO_2$, the charge-discharge kinetics and material stability of these materials continue to be of concern.
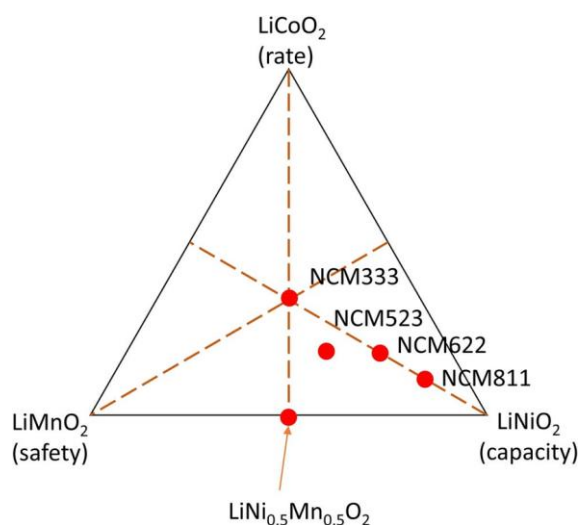
Figure 3 Phase diagram of the ternary system between LNO, LCO and LMO [16]

Recent studies [17,18] showed that Li-rich materials (common seen as $aLiNi_xCo_yMn_zO_2$ - $(1-a)Li_2MnO_3$), which also crystallized into layered structure, have been thought of as interesting cathode candidates for next generation lithium-ion batteries, as a result of their high capacities, low cost and good thermal stability. However, there are still several challenges to their practical uses, such as their high initial irreversible capacity, poor cycle stability, low-rate capability, and significant voltage, capacity, and energy degradation during cycling. In addition, the choice of the active transition metals is limited to mixtures of Ni, Co, and Mn since it is necessary to provide a stable layered structure during charge and discharge in order to achieve appropriate lithium transport characteristics [19]. Replacement of small amount of transition metals (often in the region of 1 - 5% by weight), so called doping or substitution, might be useful to improve the material's overall performance [20,21], the limited element selection still continuous promotes the price of this type of cathode materials and potentially cause shortages, particularly for the less accessible Ni and Co in the near term.

With less restrictions on the active redox element, a new family of cation disordered rocksalt (DRX) cathodes has recently gained a lot of scientific interests. They can use a variety of cheap and easily available transition metals, such as Mn, Fe, Ti, and V, which significantly increases the longevity of lithium-ion batteries while lowering the cost of their components [22].

III-3 Appearance of DRX

Cation disordered rocksalt (DRX) lithium transition metal oxide (LMO) cathodes have a crystalline rocksalt structure and a disordered arrangement of lithium (Li) and transition metals (TMs) at the octahedral cation sites in a simple face-centered cubic (FCC) anionic sublattice (Figure 4). This is considered as the significant difference in comparison to the ordered layered structure, in which Li and TM are arranged layer by layer alternatively. Thus, DRX compounds can be made of a wide range of transition metal species since no particular order is required, which can have long-term advantages for the lithium battery industry by reducing its dependence on expensive and rare raw materials [23]. The development of DRX cathodes can be traced back to the late 20th century when researchers began exploring alternative materials to enhance the performance of rechargeable batteries. Traditional cathode materials, such as layered oxides and spinel structures, were limited by their inherent limitations, such as limited energy density and voltage fade over repeated charge-discharge cycles [24].

Initially, cation disorder has long been thought to be electrochemically inactive and destructive to Li+ transport and, consequently, to the reversible capacity of intercalation-type electrodes [24]. The disordered arrangement of cations within the rock-salt crystal structure was believed to hinder the mobility of ions and compromise the overall battery performance. Consequently, these materials were largely overlooked in favor of more structurally ordered compounds. Nevertheless, a number of recent theoretical and experimental studies have shown that DRX cathodes are feasible [25,26,27]. The unique structural features of DRX cathodes enable facile diffusion of lithium ions within the material, allowing for rapid charge and discharge processes. Additionally, the disordered cation arrangement offers greater flexibility for accommodating volume changes during cycling, reducing mechanical stress and enhancing the overall durability of the cathode.

The discovery of the electrochemical potential of cation-disordered rock-salt cathodes has opened up new possibilities for the design of advanced rechargeable batteries. These cathodes hold great promise for next-generation energy storage devices, such as

lithium-ion batteries, as they offer the potential for higher energy densities, improved safety, and prolonged cycle life.
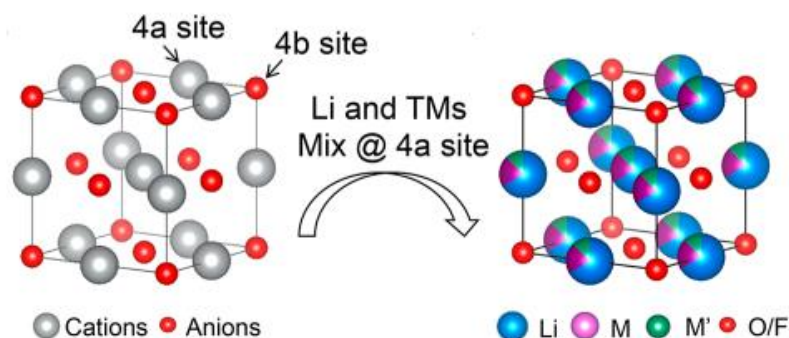
Figure 4 Schematics showing the crystal structure of (Left) a classic rocksalt and (Right) a cation-disordered rocksalt [28].

III-4 Properties of DRX

a) Li+ Mobility

Li+ diffusion between two octahedral (O) sites in rocksalt-type LMOs goes through an intermediary tetrahedral (t) site, also known as O-t-O diffusion (Figure 5) [29]. The Li+ diffusion barrier is significantly influenced by the size of the tetrahedral site (T_d) as well as the electrostatic interaction between Li+ in the activated T_d site and the four transition-metal cations arranged in face-sharing octahedra to form a so-called "tetrahedral cluster" (Figure 6.a) [30]. Therefore, an approach to enhance Li diffusivity may concentrate on decreasing the size of the tetrahedral site as well as the number of nearby transition-metal cations, so minimizing their contributions to the activation energy.
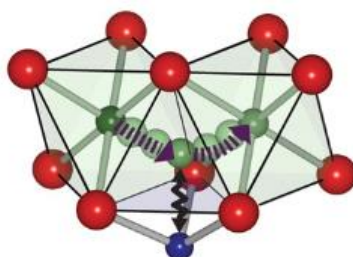
Figure 5 O-t-O Li+ diffusion where encountering a strong repulsion from a nearby transition-metal cation [30].

Theoretically, there can be five different forms of tetrahedral clusters when the cation lattice is saturated with Li and M species: Li_4, Li_3M, Li_2M_2, LiM_3 and M_4 (0-TM, 1-TM, 2-TM, 3-TM and 4-TM channels respectively). LiM_3 and M_4 environments are instantly ruled out as potential O-t-O Li^+ diffusion pathways because Li^+ diffusion requires at least two O_h Li to be linked via the active T_d site [31]. In stoichiometric layered lithium metal oxides, every tetrahedral site is coordinated by either 1-TM channels that promote Li^+ migration or 3-TM channels that do not participate in Li^+ diffusion [32]. On charge, Li^+ are extracted so that all Li previously filling the face-sharing octahedral sites are eventually emptied. The migration barrier for 1-TM channels is extremely sensitive to the occupancy of sites close to the intermediate T_d site of the hop during this emptying process. Due to the strong coulombic contacts created by the single vacancy hop between Li^+ in the activated site and Li^+ in the face-sharing octahedral site, the barrier for hops into isolated vacancies is much higher than for di-vacancy hops. The di-vacancy hop, on the other hand, lacks this repulsion and has a reduced Li^+ diffusion barrier as a result (Figure 6) [33].
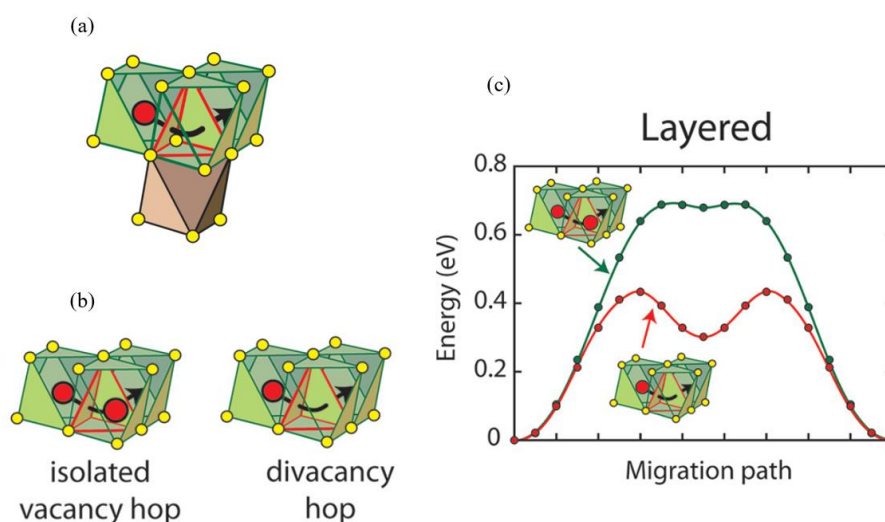
Figure 6 (a) Tetrahedral cluster (1-TM channels). (b) & (c) The isolated vacancy hop and the divacancy hop with their corresponding energy barrier for layered Li_xMO_2 [33].

The disordered rocksalt structure (DRX), in contrast to the layered oxides, where Li^+ diffusion is only taking place through the 1-TM channels as discussed thus far, would be expected to have very little Li^+ mobility because of the major reduction of the slab spacing and size of the Td site as a result of cation mixing [34]. Although disordering

results in poor Li^{+} diffusion along 1-TM channels, it also creates active 0-TM channels. In 0-TM channels, the lack of transition metals in face-sharing octahedra reduces the electrostatic repulsion in the activated Li site, resulting in improved Li^{+} transport [34].

Figure 7 illustrates the mean migration barriers in the 0-TM and 1-TM channels as a function of the typical tetrahedron height of two model disordered crystals, Li_2MoO_3 and $LiCrO_2$. The mean barrier grows as the tetrahedron height (h) reduces in the red and blue dashed lines, where the face-sharing octahedral species is Mo^{4+} and Cr^{3+}, respectively. At h = 2.35 Å, the mean barrier reaches ~580 meV along a $1-Mo^{4+}$ channel and ~560 meV along a $1-Cr^{3+}$ channel, with the awareness that these barriers tend to get stronger as the oxidation state of the transition metal gets higher. [34,35]. The large barriers in disordered lithium metal oxides show the highly limited Li^{+} diffusion along 1-TM channels that was stated earlier when compared to the typical 1-TM barriers in layered oxides (300 meV) [36] because of the electrostatic repulsion on the activated T_d Li^{+} [34,35].
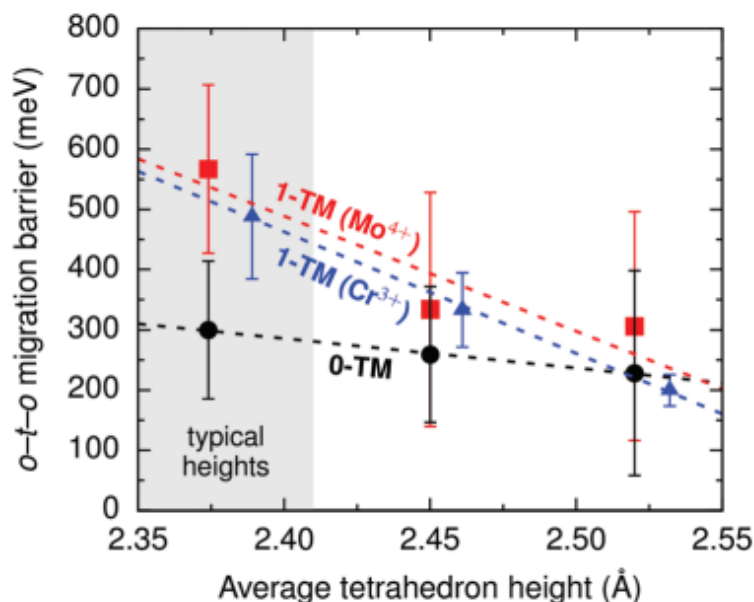
Figure 7 Calculated Li migration barriers along 1-TM and 0-TM channels as a function of the average tetrahedron height in model disordered Li_2MoO_3 and $LiCrO_2$ structures [34,35].

In contrast, even for a short average tetrahedron height (h = 2.35 Å), the mean migration barrier for 0-TM channels does not approach 300 meV. This is due to the much lesser electrostatic repulsion on the activated T_d Li^+ caused by the face shared octahedral Li^+ (compared to $Mo4^+$ or $Cr3^+$) [34]. The energy of the 0-TM T_d site gradually decreases as Li is removed from nearest-neighbor octahedral sites during charge, stabilizing T_d Li after all face-sharing octahedral Li sites are empty. The comparatively low barrier for Li migration between two 0-TM T_d sites, which is estimated to be ~415 meV, allows the Li to escape the T_d sites formed at the completion of charge [34,35].

In conclusion, microscopic O-t-O Li^+ diffusion occurs in layered Li_xMO_2 compounds through a Li di-vacancy mechanism and relies on 1-TM channels, with the Li^+ diffusion coefficient being influenced by the distance between the Li slabs and the oxidation state of the transition metal which faces-sharing Li^+ in the activated site. Contrarily, in DRX compounds, Li^+ migration is generally influenced by 0-TM channels, with a diffusion barrier that is essentially independent of the average tetrahedron height and the composition of the transition metals.

b) *Excess Lithium*

In DRX, the microscopic diffusion 0-TM channels must connect to one another or create a percolating network throughout the structure in order for the macroscopic Li^+ diffusion to occur. In particular, Li^+ diffusion will be restricted to isolated percolating regions inside the structure and does not result in a detectable macroscopic current if these channels do not form a continuous network [31,34,35]. Most ordered structures have small unit cells, making percolation visible. In comparison, disordered systems have environments distributed statistically, making it more difficult to identify when exactly percolation is achieved. In a cation disordered structure, macroscopic Li^+ diffusion pathways are less visible, which explains why DRXs were long thought to be electrochemically inert and weren't shown to be percolating until recently [31,34,35].

As 0-TM channels indicate a local domain rich in lithium, their concentration will rise as lithium content does (x in $Li_xM_{2-x}O_2$). Other investigations [31,34,35,37] looked at how cation disorder and Li content x affected Li percolation in the DRX structure using only

0-TM channels. The likelihood of discovering a percolating network of 0-TM channels in a rocksalt-type LMO is illustrated in Figure 8 as a function of Li concentration (x) and cation mixing (%). Along the black line (percolation threshold), the percolation probability jumps sharply from 0 (red) to 1 (blue). This threshold at which a percolating network of 0-TM channels is established is known as the critical Li concentration (x_c). The critical Li concentration varies in Figure 8, from x_c ~ 1.13 for layered oxides (0% cation mixing) to x_c ~ 1.09 for totally disordered oxides (100% cation mixing) [34].
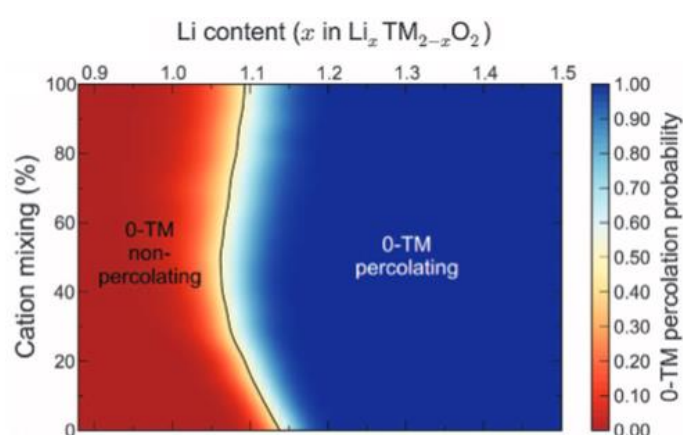
Figure 8 Probability of finding a percolating network of 0-TM channels versus Li content and cation mixing [34].

Investigating how Li excess and cation mixing impact the Li content in the network by changing the lithium concentration to lithium atoms per formula unit (Accessible lithium), a more typical notation in electrochemistry. The "inaccessible" Li must go through 1-TM or 2-TM channels in order to reach the percolating 0-TM network, whereas the "accessible" Li can diffuse through the network without doing so. Figure 9 shows the available Li content per formula unit as three black lines (0.8 Li, 1 Li, and 1.2 Li). Accessible Li content steadily rises when x exceeds ~1.09 (the percolation threshold) and becomes as high as 1 Li as x surpasses ~1.22 irrespective of the presence of cation mixing [34]. More 0-TM channels are added to a percolating 0-TM network when Li excess increases, increasing the network's conductivity.

Moreover Urban *et al.*'s study [31] demonstrates that the critical lithium concentration rises to $x_c = 1.092$ when only 0-TM channels are anticipated to be active, requiring 9%

excess lithium to achieve percolation (as opposed to $x_c = 0.662$ for a network of active 1-TM and 0-TM channels), and for 1 lithium atom per formula unit to become accessible by 0-TM network the excess lithium required is more than 25% ($x_c = 1.257$) (Figure 10).
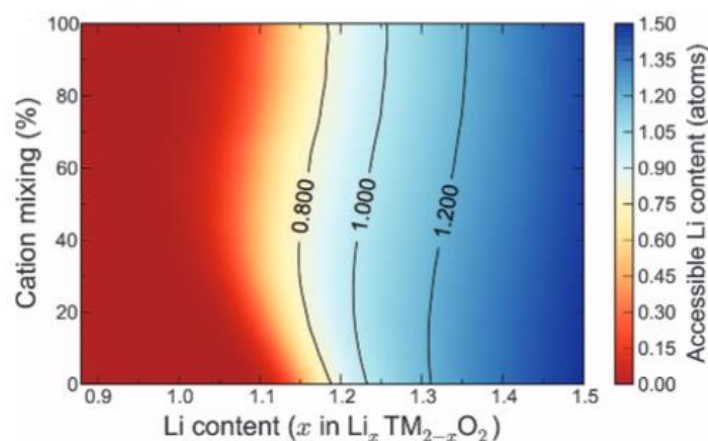
Figure 9 Accessible Li content by a percolating 0-TM network versus Li content and cation mixing [34].
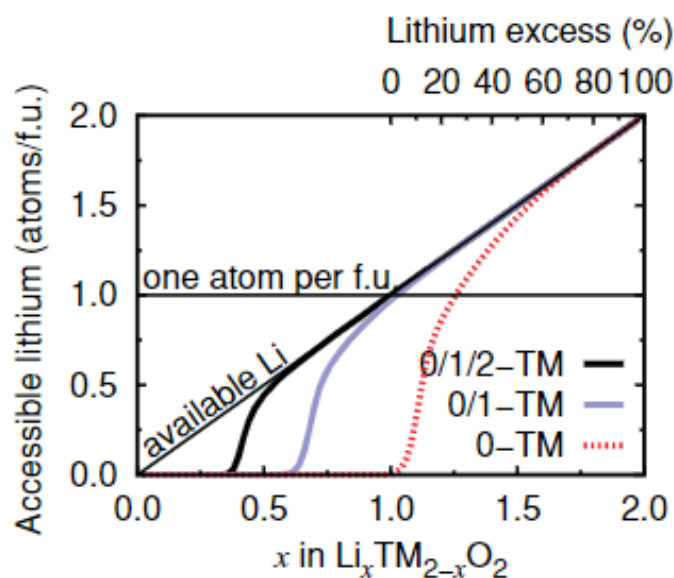
Figure 10 Accessible amount of lithium as function of the overall lithium content [31].

In conclusion, long-range 0-TM Li$^+$ diffusion can be maintained by DRXs as long as Li is present in excess (Li/M > 1). In order to have Li percolation, only 10% Li excess is required, while for 1 Li per formula unit extraction needs about 26% Li excess. It is

crucial to keep relatively low Li excess quantities in these materials because too high Li/M ratio leads to restricted transition metal redox capacity, which is swapped for O anion-redox capacity, this has a detrimental effect on the cathode's energy density and the overall reversibility of the charge compensation mechanisms during cycling.

c) *Short-Range Order (SRO)*

While Li transport depends on the percolation network and purely determined by statistical effects, cation short-range order (SRO) is crucial in determining the amount of kinetically extractable Li in DRX materials. Performance can be significantly impacted by these small variations from randomness that are undetectable by standard X-ray diffraction (XRD) [38]. According to various research [39,40,41], SRO is common in DRX cathode materials and varies significantly depending on the TM species present, moreover, it may have a major impact on Li$^+$ transport, enhance or diminish overall Li percolation depending on the nature of Li network, offering another way to alter their performance.

Ji *et al.*'s study [42] compared a two Li-excess DRXs, $Li_{1.2}Mn_{0.4}Ti_{0.4}O_2$ (LMTO) and $Li_{1.2}Mn_{0.4}Zr_{0.4}O_2$ (LMZO). Since Zr^{4+} and Ti^{4+} are isoelectronic and their only function is to charge compensate for the excess Li, it would be reasonable to predict that these materials, based on their chemical similarities, would have almost identical electrochemical properties. In fact, the larger ionic radius of Zr^{4+} should lead to a bigger lattice parameter for LMZO, which is typically thought to be advantageous for Li mobility. Yet, the study finds that LMTO performs significantly better than LMZO, which goes against these assumptions. They demonstrate using a combination of calculations, measurements, and electron diffraction that the performance difference between LMTO and LMZO is caused by various cation SROs, which regulate the connectivity and population of Li migration channels.

Both of these compounds include the same amounts of Li and Mn as well as equal amounts of the high-valent d^0 cations ($Ti4^+$ and $Zr4^+$). The black electrochemical curves in Figure 11(a) demonstrate that while 0.79 Li per formula unit (f.u.) can be reversibly withdrawn from or injected into LMTO at room temperature, this value decreases to

roughly 0.52 Li per formula unit (f.u.) for LMZO under the same circumstances [35,42]. Figure 11(b) shows the LMTO and LMZO electron diffraction (ED) patterns. In addition to the circular spots that may be associated with a DRX structure, we also see diffuse scattering patterns around those spots, indicating the presence of SRO and showing that the two as-synthesized compounds have various degrees and types of SRO [35,42].
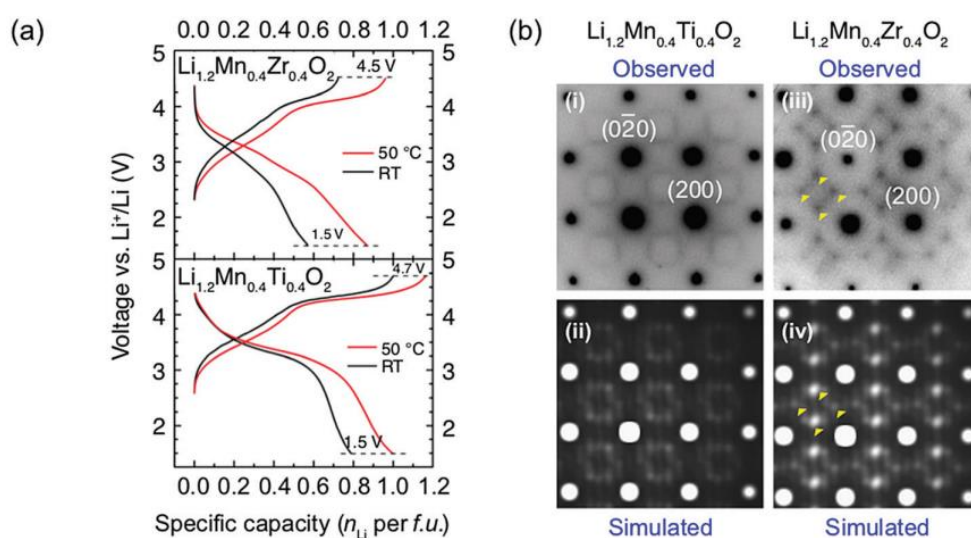
Figure 11 (a) First cycle galvanostatic voltage profiles of LMZO and LMTO at 50 °C and room temperature. (b) ED patterns of LMTO and LMZO along the zone axis [100] [35].

In summary, DRX structures may show some degree of SRO rather than a completely random arrangement of cations, and this SRO can be changed to influence the transport properties.

As with anything in this life, this kind of cathode material has a variety of issues. Starting with voltage variations that leads to a broadening or shifting of the voltage plateau, which reduces energy density and makes it challenging to maintain a stable voltage output. Additionally, cation disorder disrupts the diffusion pathways for ions within the material, decreasing ionic conductivity and limiting the rate capability of the cathode. This, coupled with potential phase separation and altered electrochemical

stability, can result in poor cycling performance, capacity fading, and decreased overall efficiency of the cathode material.

III-5 Strategies to improve DRX

In the field of advanced battery technologies, the presence of cation disorder in rock salt cathode materials has emerged as a significant hurdle in achieving high-performance energy storage systems. The detrimental effects of cation disorder, including voltage variations, hindered ion diffusion, and compromised electrochemical stability, have limited the full potential of rock salt cathodes. To overcome these challenges and improve the performance of cation disorder rock salt cathodes, researchers have been actively exploring innovative strategies that enhance structural stability, promote efficient ion mobility, and optimize electrochemical properties. This section will delve into a selection of these strategies, elucidating their underlying principles and discussing their potential efficacy in improving the performance of cation disorder rock salt cathodes.

a) Carbon Coating

By altering the surface chemistry or adding protection layers to reduce direct contact between the active material and the electrolyte, surface coating is a practical and affordable approach to enhance battery performance [43,44]. By carefully choosing the coating materials, it is possible to create coating layers that can increase structural stability, reduce transition metal dissolution, and favor the creation of solid electrolyte-interface (SEI) films, as well as ionic or electronic conductivity. Additionally, the electrode resistance, side reactions, and generation of heat during cycling are reduced, which has a notable impact on the first cycle's coulomb efficiency as well as cycle life, rate capability, and reversible capacity [45]. The coating materials that have been researched up to this point include carbon, metal oxides, metal phosphate, metal fluoride, metal oxyfluoride, and glass composite. Due to the numerous benefits that come from the special chemical and physical characteristics of carbon, carbon coating contributes an exclusive part in anode materials and is becoming increasingly significant in the advancement of cathode materials [46].

A material's surface is better protected from chemical deterioration when it is carbon coated. Poor cell lifetimes in LIB batteries are mostly caused by side reactions at the electrode-electrolyte interface (Figure 12a). Preventing material degradation as a result of the lattice expansion during lithium intercalation is also one of the main functions of carbon coating. In this situation, the carbon material stops the cycling from causing the active material's particle connections to break down (Figure 12b). Additionally, by improving the conductivity of the electrode material, the carbon coating may speed up the supply of lithium to the electrode material particles. In this scenario, a quick transfer of lithium and electrons is made possible by the carbon shells of the electrode material particles intersecting or coming into touch with one another (Figure 12c) [47].
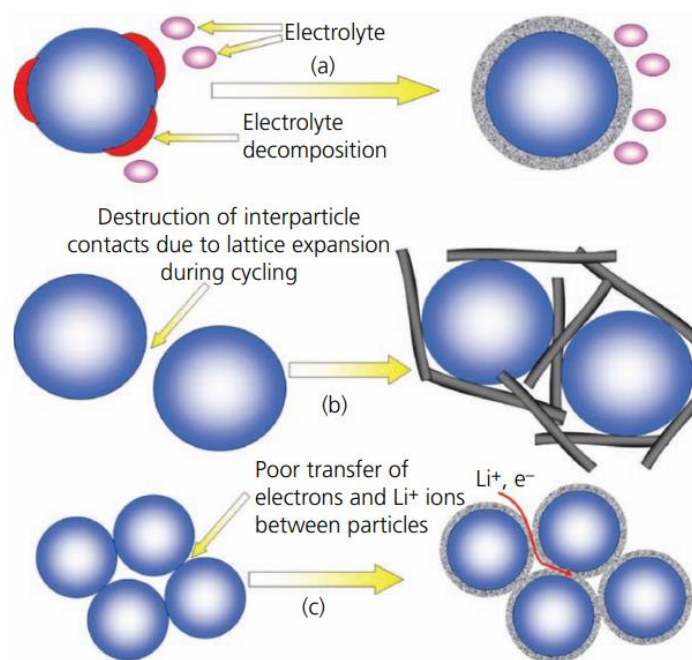
Figure 12 Main functions of carbon coating: (a) prevention of the electrolyte decomposition, (b) buffering of lattice expansion during cycling and (c) increasing the surface conductivity.

b) *Cation Vacancies*

The physicochemical characteristics of the active electrode materials, such as their morphologies [48], porosities [49], crystal structures [50], and electrical conductivity [51], heavily influence the electrochemical performance. Despite the benefits of using TMOs for energy storage, there are still a number of challenges associated with their use. For

example, i) since the majority of studied oxides are semiconductors with wide bandgaps, they frequently display poor electrical conductivity, which is detrimental for achieving good electrode performance [52,53]. ii) Ion diffusion kinetics are often poor in metal oxides [54]. iii) The TMOs often experience considerable volume contraction/expansion upon charge/discharge when employed as battery electrodes [55,56].

One of the widely employed methods to address and mitigate the above-mentioned issues is to combine transitional metal oxides (TMOs) with conducting materials or other metal oxides to improve the electrical conductivity and electrochemical reactivity [57,58,59,60]. This methodology is "extrinsic," meaning that the host materials' atomic structures are not changed as a result of the modification. Consequently, the electrode properties are typically changed by increasing the surface area to encourage ion absorption or by making combinations with conductive materials to increase electrical conductivity. Despite this, the improvement in electrode performance is only minor [61].

A revolutionary "intrinsic" method that involves purposefully introducing flaws into the lattice structure of host materials has drawn growing interest in the past few years. The recently introduced defects-engineering-based "intrinsic" approaches, in comparison with "extrinsic" methods, primarily rely on modifying the local atomic structures of electrode materials in a manageable way, which further permits adjusting the electronic and structural properties in an efficient manner, realizing enhanced electrochemical efficiency by reducing diffusion energy barriers, providing more intercalation sites, and enhancing electrode kinetics [62,63]. In general, there are many various kinds of intrinsic defects present in materials, such as cation vacancies, anion vacancies, vacancy clusters [61], and plenty of lattice defects, such as lattice distortion [64], stacking faults [65], and twin boundaries [66]. Due to their ease of integration, controllability, and beneficial impacts on electrochemical intercalation, vacancy-related defects are more advantageous than the others.
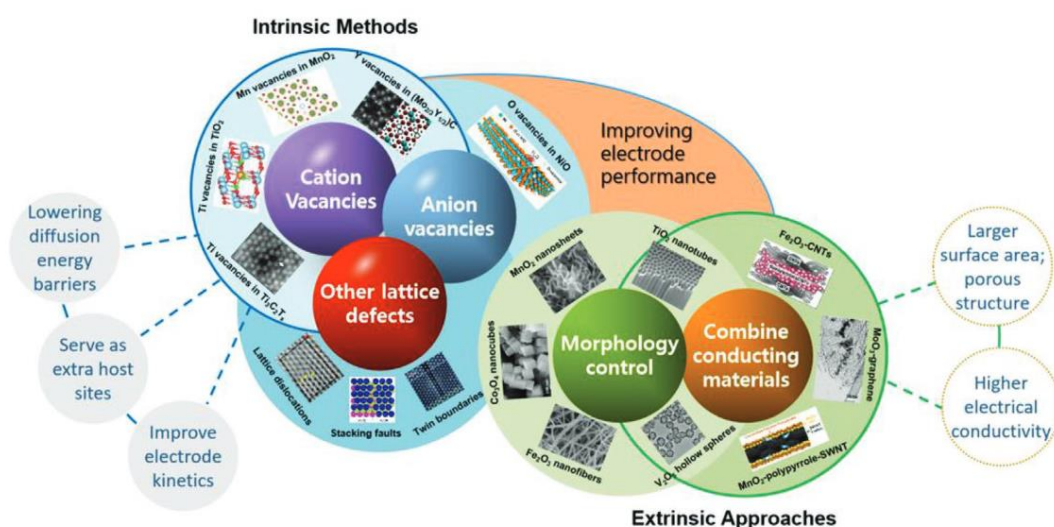
Figure 13 Schematic diagram showing the "extrinsic" and "intrinsic" approaches for improving the electrochemical energy storage performance.

As was previously established, Li diffusion in DRX is only possible between two octahedral sites via activated tetrahedral sites with no face-sharing TM cations, or 0-TM channels. A 0-TM percolation network is needed throughout the structure for a bulk scale Li transport; this percolation is regulated by the number of 0-TM channels and how they are arranged, both of which are affected by the cation SRO [67]. This cation SRO in DRX is influenced by a variety of factors, including charge balance and the difference in ionic radius. One way is that the high-valent TMs (such Mn^{3+}, Ti^{4+}, and Nb^{5+}) in DRXs have a tendency to reject one another and mix tightly with Li^+ to maintain local electroneutrality, which prevents Li separation hence reduce 0-TM formation. The size mismatch between high-valent TMs and Li^+, on the other hand, promotes Li separation to reduce strain and opposing the charge effect hence promote 0-TM formation [27]. Huang *et al.*'s study [68] demonstrates that the SRO of materials, which are supposed to be identical, can also be easily influenced by creating a shortage of Li during the manufacturing process. This new technique can be employed to improve the capacity and rate performance of DRX cathodes.

IV. OBJECTIVES

The primary objective at hand is to discover a straightforward and efficient approach for preparing DRX cathode materials for LIBs. The focus lies on devising a method that is both low cost and easy to implement during the manufacturing process. Additionally, energy efficiency plays a crucial role in our pursuit, aiming to minimize resource consumption and reduce environmental impact. By seeking a streamlined solution, I strive to unlock the potential for widespread adoption and accessibility, ensuring that the benefits of these materials can be realized across various industries and applications.

To achieve this objective, we are exploring the utilization of mechanochemical milling as an alternative to conventional synthesis methods of cathode materials, such as direct solid state reaction, sol-gel method, co-precipitation method etc. Mechanochemical milling involves the mechanical activation of the materials through grinding or milling, leading to chemical transformations at the molecular level. This method offers several advantages over traditional techniques. First, it eliminates the need for complex and resource-intensive reaction conditions, such as high temperatures or harsh solvents. By relying on mechanical forces, mechanochemical milling simplifies the preparation process, making it more accessible and cost-effective. Second, this technique often yields superior product quality with enhanced purity and crystallinity. Moreover, mechanochemical milling is known for its energy efficiency, requiring significantly lower energy inputs compared to other methods. This not only reduces environmental impact but also contributes to the overall sustainability of the manufacturing process. By embracing mechanochemical milling, we are paving the way for a simpler, more efficient, and environmentally conscious approach to material preparation.

Another crucial objective is to enhance the electrochemical performance of these materials through specific methods, such as cation vacancies and fluorine substitution. Introducing cation vacancies, as mentioned before, involves intentionally creating spaces within the crystal lattice by removing certain ions. This approach can lead to improved lithium-ion diffusion ability and ionic conductivity, enhancing the

material's performance in applications such as batteries or fuel cells. Additionally, fluorine substitution involves replacing certain anionic atoms with fluorine atoms. This modification can alter the material's electronic structure, resulting in improved stability, higher catalytic activity, or enhanced optical properties. By strategically employing these techniques, the aim is to unlock the untapped potential of these materials, boosting their efficiency, durability, and functionality. Ultimately, by focusing on the incorporation of cation vacancies and fluorine substitution, we strive to push the boundaries of material performance and enable groundbreaking advancements in various technological domains.

V. EXPERIMENTAL SECTION

V-1 Materials Preparation

Base line material $Li_{1.25}Fe_{0.5}Nb_{0.25}O_2$: The $Li_{1.25}Fe_{0.5}Nb_{0.25}O_2$ compound was synthesized using a solid-state method. Initially, stoichiometric amounts of Nb_2O_5, Fe_2O_3, and Li_2CO_3, along with 10 wt% excess of Li_2CO_3 to compensate for lithium loss during synthesis, were mixed with anhydrous ethanol as solvent using mechanical ball milling for 4 hours at 400 rpm. The resultant mixture was subsequently dried in an air oven. Next, the dried mixture was pressed into a round pallet and heated at 900°C for 12 hours in air using a muffle furnace. The heating process involved a ramp-up rate of 300°C/hour for 3 hours until reaching 900°C, holding at 900°C for 12 hours, and then dropping down to 90°C at the same rate of 300°C/hour. Finally, the synthesized samples were finely ground using an agate mortar to prepare them for the carbon coating step.

Dry ball milling prepared sample 0%, and those with 2% and 6% Cation Vacancies: The synthesis process of $Li_{1.25}Fe_{0.5}Nb_{0.25}O_2$, $Li_{1.2}Fe_{0.5}Nb_{0.26}O_2$, and $Li_{1.1}Fe_{0.5}Nb_{0.28}O_2$ compounds with 0%, 2%, and 6% cation vacancies, respectively, is via mechanochemical dry ball milling. Stoichiometric amounts of Nb_2O_5, Fe_2O_3, and Li_2O (with 10 wt% excess of Li_2O to compensate for lithium loss during synthesis) were employed as precursors. These precursors were dispersed in Ar-filled zirconium jars and then subjected to planetary ball milling (PLANETARY MICRO MILL

PULVERISETTE 7) at different rotational speeds and durations as per the experimental plan, which will be discussed later in this thesis. Each jar contained ≈2.5 g of total precursor material, and the grinding media consisted of 16 large (10 mm diameter), 15 medium (5 mm diameter), and 15 small (3 mm diameter) zirconium balls, resulting in a balls-to-materials weight ratio of approximately 23:1.

Carbon Coating: To prepare the carbon coated samples $Li_{1.25}Fe_{0.5}Nb_{0.25}O_2/C$, $Li_{1.2}Fe_{0.5}Nb_{0.26}O_2/C$, and $Li_{1.1}Fe_{0.5}Nb_{0.28}O_2/C$, the as prepared 0%, 2% and 6% samples were mixed with carbon black in a weight ratio of 90:10 wt% using a planetary ball mill at a speed of 750 rpm for a duration of 4 hours. The mixing process was carried out in zirconium jars, utilizing zirconium balls as the griding media with a weight of 10~15 times that of the material.

V-2 Electrochemical Measurement

To prepare the positive electrode, a mixture containing 80 wt% of active material, 10 wt% of carbon black (Tmax), and 10 wt% of polyvinylidene fluoride (PVdF, Tmax) pre dissolved in N-methyl-2-pyrrolidone (NMP) (5% wt) was subjected to planetary ball mill at a speed of 250 rpm for a duration of 2 hours. Additional NMP was added to adjust the viscosity of the slurry. This mixture was then pasted onto an aluminum (Al) foil current collector. Subsequently, the electrode was subjected to overnight drying in a vacuum oven maintained at 120°C and punched into discs of 13 mm diameter.

The coin cell assembly process was performed within an argon-filled glove box, utilizing the prepared cathode disc, a glass microfiber separator, a Li-metal foil (employed as the negative electrode), spacers, springs and an electrolyte comprising 1 M $LiPF_6$ in a 1:1 (volume ratio) blend of ethylene carbonate (EC) and dimethyl carbonate (DMC). Figure 14 shows how the assembly process of a coin cell is done. The initial step involves positioning the negative case (anode) and then carefully placing the spring followed by the spacer in order to secure the internal components of the cell. Subsequently, the Li foil is placed, serving as the anode, and electrolyte is added onto it. A glass fiber separator is then inserted to prevent physical contact between the anode and cathode while facilitating ion transport within the cell. Additional

electrolyte is applied before the cathode is positioned on top of the soaked separator, facing downward. Finally, the positive case (cathode) is added, preparing the cell for subsequent sealing procedures.
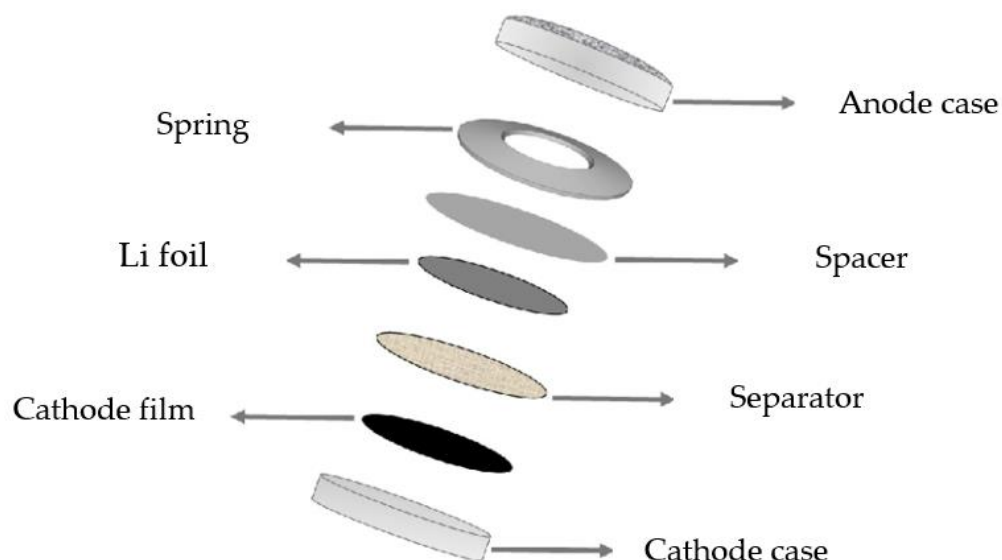
Figure 14 Scheme for the coin cell battery components used in order.

Finally, the assembled CR2025-type coin cells were tested under room temperature conditions using the Neware battery test instrument between 1.5V and 4.8V at different C-rates.

As part of the electrochemical measurement, a charge/discharge test was conducted on the coin cells at constant currents. The specific current for the test was calculated based on the amount of active materials present in the cathode electrode. By applying a constant current, the cell voltage increased continuously till the upper cut-off voltage (4.8V), and then discharged at the same current until the predefined cutoff voltage (1.5 V) was reached. This test allowed for the evaluation of the cell performance, including its capacity retention, energy efficiency, and cycling stability, providing valuable insights into the electrochemical behavior and performance of the DRX materials.

Another important aspect of the electrochemical measurement is the determination of the differential capacity, represented as dQ/dV versus voltage. This measurement involves plotting the rate of change of charge (dQ) with respect to voltage (dV) as a

function of the applied voltage. By analyzing this curve, valuable information about the electrochemical processes occurring within the battery can be obtained. The differential capacity profile provides insights into various phenomena, including the occurrence of redox reactions, phase transitions, and electrode/electrolyte interfacial dynamics. It serves as a valuable tool for characterizing the electrochemical behavior and performance of the battery system, aiding in the understanding and optimization of its operation.

Finally, cyclic voltammetry (CV) was employed as a technique that involves applying a triangular or sawtooth potential waveform to an electrochemical cell and recording the resulting current as a function of the applied potential. By sweeping the potential back and forth, valuable information about the redox reactions, electron transfer kinetics, and electroactive species in the system can be obtained. Cyclic voltammetry provides insights into the electrochemical behavior and characteristics of the system, including the identification of oxidation and reduction peaks, determination of reaction mechanisms, assessment of electrode performance, and investigation of surface properties.

V-3 Materials Characteristics

The X-ray Diffraction (XRD): XRD analysis is a valuable technique used to examine the cathode structure in Li-ion batteries. It helps identify the crystalline phases present, analyze crystallographic parameters like lattice parameters and crystal size, track phase transitions during charge/discharge cycles, detect impurities or secondary phases, and understand the electrochemical performance and stability of the cathode materials. XRD provides important insights into the structural properties of synthesized cathode materials, facilitating the optimization of synthesis processes, quality control, and the development of improved battery materials. The experiments have been acquired on a Rigaku Smartlab instrument, exploiting Cu Kalpha radiation in the angular range 5-90 deg with step size 0.02 and 0.8 deg/min.

Scanning Electron Microscopy (SEM) image: Besides the cathode structure and crystallinity, the size and morphology of nanoparticles are crucial factors influencing

the performance of cathode materials in Li-ion batteries. To analyze these characteristics, scanning electron microscopy (SEM) is employed to examine the surface morphology of the cathode materials. SEM allows for the assessment of particle size, shape, and distribution, providing insights into the agglomeration of particles, which affects the porosity of the electrode and the pathways for ion diffusion. SEM also aids in evaluating the uniformity and quality of surface coatings, identifying contaminants, and detecting side reactions that can impact the overall battery performance. Furthermore, SEM assists in failure analysis by detecting structural changes and provides valuable information for material optimization and improving the electrochemical performance of the cathode materials.

Energy dispersive X-ray (EDX) element mapping: EDX analysis is conducted on cathode materials to analyze their elemental composition, identify phases, map elemental distributions, detect defects, and contribute to the design and optimization of cathode materials for energy storage applications. By providing information about the presence and distribution of specific elements, EDX mapping aids in understanding the composition, stoichiometry, and homogeneity of cathode materials. This knowledge is crucial for studying their electrochemical behavior, optimizing synthesis methods, and improving performance and stability in energy storage devices such as batteries.

VI. ELECTROCHEMICAL PERFORMANCE OF BASE LINE MATERIAL

The preparation of baseline materials ($Li_{1.25}Fe_{0.5}Nb_{0.25}O_2$) is done using the traditional method of synthesizing cation disorder rock-salt cathodes suggested by the literature. The aim is to establish a reference dataset that can be later compared to the new synthesis method that needs to be explored. The traditional synthesis process involves wet mechanical milling, followed by the calcination process in air using a muffle furnace. By following this established procedure, we can obtain a set of well-characterized materials with known properties. These materials will serve as a benchmark to evaluate and compare the performance and properties of the new

synthesis method, enabling us to assess its effectiveness and potential for further improvements.

VI-1 Electrochemistry

To begin with, the type of separator that has better compatibility with DRX electrodes are demonstrated. Two different separators, i.e., Celgard® 2500 Monolayer Microporous PP Membrane and Whatman glass fiber, are employed in this thesis. The charge/discharge curves and corresponding differential (dQ/dV) curves of $Li_{1.25}Fe_{0.5}Nb_{0.25}O_2$/C (base line) material cycled with these two separators are shown in Figure 15. With a charge cutoff voltage of 4.8 V, no small plateau is observed in both discharge curves (Figures 15a and b) at a voltage above 3.5 V (R0), the absence of this discharge plateau indicates that no reduction process of Fe^{4+} to Fe^{3+} occurred. This finding agrees well with pervious report that, Fe^{4+}/Fe^{3+} reduction gradually decrease as the charge cutoff voltage increases, as demonstrated by Luo *et al* [69]. Below 3.5 V and above 2.6 V, two discharge plateaus (R1 and R2) are observed representing reduction processes, which will be explained in the next paragraph. Finally, below 2.6 V, R3 discharge plateau shows that Fe^{3+} is reduced to Fe^{2+}. The result suggests that Fe^{3+} is first oxidized and then reduced in the initial charge process. Even though the reduction of Fe in the charging process is abnormal, it can be explained by the redox mechanism.

When the voltage reaches approximately 4.15 V during initial charge, there is a noticeable charge plateau indicating the oxidation of Fe^{3+} to Fe^{4+}. Beyond 4.15 V, the curve returns to its original position, suggesting the reduction of Fe^{4+}. Throughout the discharge process, the valence state of Fe remains unchanged until it reaches 2.6 V. Between 2.6 V and 1.5 V, the reduction of Fe^{3+} to Fe^{2+} occurs. The negligible change in the valence state of Fe above 2.6 V during discharge suggests that Fe does not contribute significantly to the high discharge capacity. Since Nb is electrochemically inactive in this voltage range, the discharge capacities are likely derived from the reduction of oxygen, as indicated by the R1 and R2 discharge plateaus. Interestingly, the unexpected reduction of Fe above 4.15 V during the initial charge also suggests that oxygen oxidation predominantly occurs between 4.15 V and 4.80 V.

In the second charge, when voltage reaches approximately 3.7 V, a reversible oxidation of Fe^{2+} to Fe^{3+} occurs. Above 3.7 V, the oxygen starts to be oxidized up to 4.8 V and displays reversible reduction during the discharge.

The differential curves (shown in Figures 15c and d) reveal distinct charge and discharge plateaus during the initial cycle. As mentioned earlier, Fe oxidation and reduction are indicated by O1 and R3, respectively. Similarly, oxygen oxidation and reduction are represented by O2, R1, and R2. Additionally, both dQ/dV curves demonstrate a flat region above 3.5 V, aligning with the charge/discharge curves where no discharge plateau is observed.
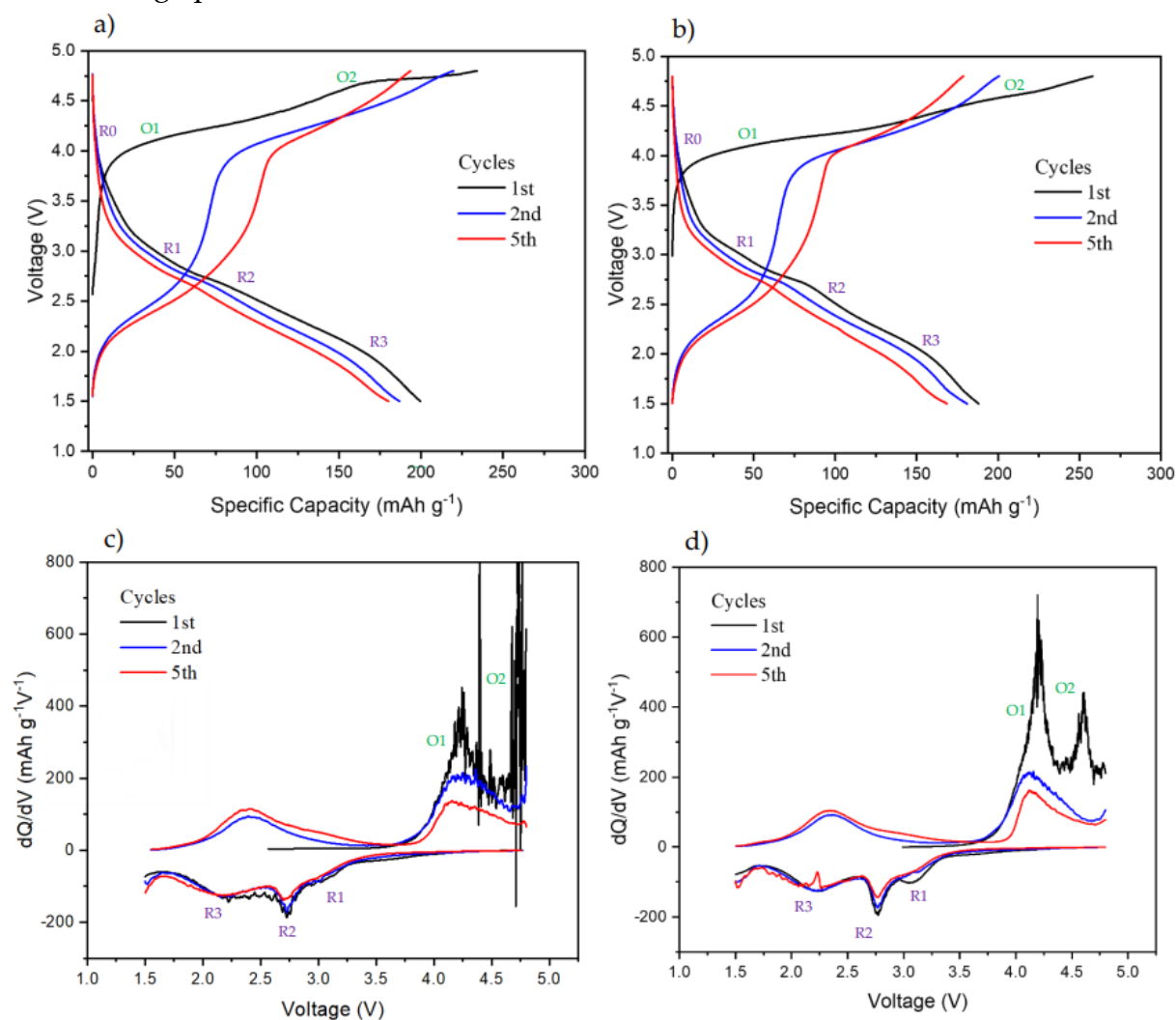
Figure 15 (a) The charge/discharge curve of Li$_{1.25}$Fe$_{0.5}$Nb$_{0.25}$O$_2$/C (Base line) with Celgard separator. (c) Corresponding differential curve of (a). (b) The charge/discharge curve of Li$_{1.25}$Fe$_{0.5}$Nb$_{0.25}$O$_2$/C (Base line) with Glass fiber separator. (d) Corresponding differential curve of (b)

The impact of redox mechanisms on electrochemical performance can be demonstrated through the dQ/dV differential curves. The R1 and R2 plateaus in Figure 16, which undergo significant changes along cycling, are associated with oxygen reduction reactions. The rapid decline of these peaks indicates the irreversible nature of oxygen redox in DRX electrodes when cycled between 1.5 and 4.8 V. The dQ/dV curve shown in the Figure reveals that the oxygen redox reaction (R2) diminishes with an increasing number of cycles. Likewise, the oxidation peaks observed in the cycling process exhibit a decreasing trend over time, suggesting that each time a gradually decreased amount of oxygen is actively participating in the oxidation reactions, reflecting its poor reversibility.
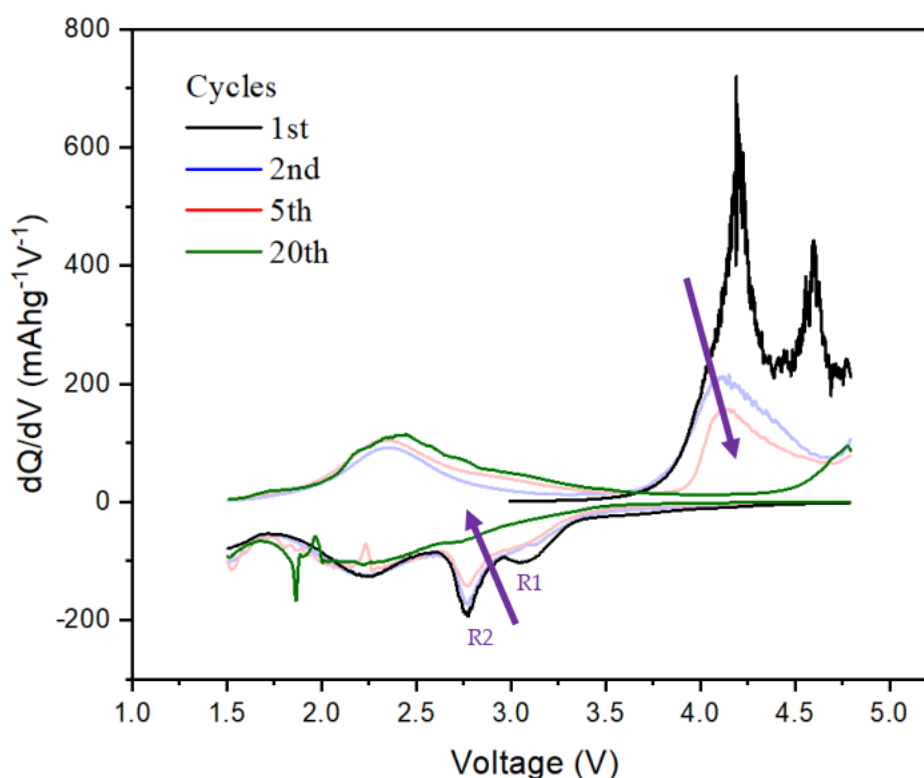
Figure 16 The differential curve of the Base line for the 20th discharge process

Figure 15 demonstrates the impact of changing the separator material from Celgard to Glass fiber on the performance of the coin cell. While the effect on discharge behavior is minimal, it has a significant influence on the charge behavior. O_2 peak is more obvious in the cell with Celgard separator during the first cycle. Besides, the other notable difference is observed in the open circuit voltage (OCV), which remains more

stable with the Glass fiber separator, maintaining it around 3 V during the initial 12-hour rest period before cycling. In contrast, the OCV of the Celgard separator cell drops to approximately 2.5 V within the same rest time period.

Moreover, the choice of separator material used has a notable effect on the oxidation reaction of Fe, as evident from the differential dQ/dV curves. With the Glass fiber separator, the peak corresponding to the oxidation reaction (O1) reaches approximately 700 mAh $g^{-1}V^{-1}$, whereas it is around 450 mAh $g^{-1}V^{-1}$ when using Celgard. This indicates that the Fe activity in that voltage region is enhanced when using the Glass fiber separator, attributed to its superior Li diffusion properties, resulting in lower resistance from the separator. Consequently, the decision to utilize the Glass fiber separator for the remaining experimental work was driven by its better Li diffusion capability, enabling greater contribution from the transition metal, and minimizing the contribution from irreversible oxygen redox.

To investigate the impact of oxygen redox on the electrochemical behavior and reversibility of the cathode during cycling, cyclic voltammetry (CV) tests were conducted. The advantage of using CV is that it allows for a comparative analysis of the kinetic of the involved redox couples, since the fixing of the amount of time at each potential is applied.

Figure 17 displays the CV curve of the baseline material, scanning from a lower cutoff voltage (LCV) of 1.5 V to an upper cutoff voltage (UCV) of 4.8 V for 5 cycles. Except for the 1st cycle, the cycling process shows relatively stable behavior, with an anodic peak (oxidation peak) observed around 2.35 V and a cathodic peak (reduction peak) centered at approximately 2.2 V. This suggests that the reversibility of the cation redox reactions of Fe (Fe^{3+}/Fe^{2+}) is compromised. On the contrary, the cathodic peak for the anodic peak at 4.3 V (the oxidation of Fe^{3+} to Fe^{4+}) is absence, indicating the reduction of Fe^{4+} to Fe^{3+} happening during charge process, which maybe overlaps with oxygen activity. Additionally, an anodic peak is observed at the upper cutoff voltage,

accompanied by a cathodic peak around 2.7 V. These peaks indicate the activation of oxygen redox reactions.

Over the course of cycling, the intensity of the oxygen oxidation peak at the cutoff voltage rapidly decreases, indicating the largely irreversible nature of the oxygen redox process. Furthermore, the anodic peak centered around 4.3 V continues to shift towards higher voltages, while the cathodic peak centered at 2.2 V gradually decreases, a weaker reduction peak around 1.8 V appears. Since these peaks originated from the oxygen redox, their degradation behavior along cycling demonstrates the occurrence of hysteresis and capacity fade on the cathode.
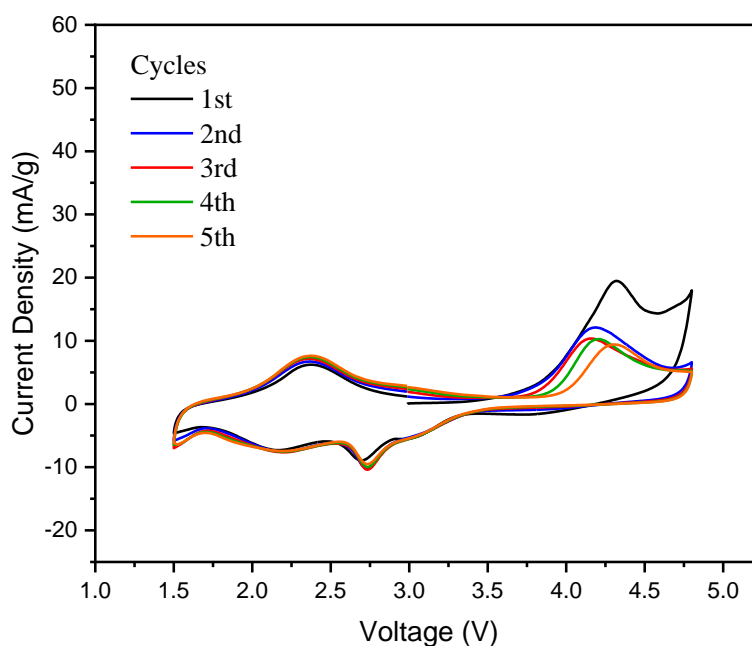
Figure 17 Cyclic voltammogram of the Base line between 1.5 V and 4.8 V at a scan rate of 5 mV min^{-1}

In contrast to the previous dQ/dV differential curves, the oxygen peaks observed on the CV graph may not appear as prominent. This is primarily due to the slow kinetics of the oxygen reaction, coupled with the relatively fast scan rate employed during the CV test. The fast scan rate prevents the materials from staying at high voltages for an extended period, where the activation of oxygen reactions typically occurs. As a result, the oxygen peaks on the CV graph may not exhibit significant magnitude or prominence.

Nevertheless, the baseline material $Li_{1.25}Fe_{0.5}Nb_{0.25}O_2$ can be synthesized via wet milling method followed by high temperature calcination. The material delivers an initial specific capacity around 200 mAh g^{-1}, however with a fast decay. The oxygen redox reactions are confirmed in this DRX material, and its poor reversibility takes the responsibility of the performance decay.

VII. SYNTHESIS OF $L_I1.25F_E0.5N_B0.25O2$ VIA MECHANOCHEMICAL BALL MILLING AND THE RELEVANT OPTIMIZATION

In this chapter, a new synthesis method being explored for cation disorder rock-salt cathodes involves dry mechanical milling and eliminates the need for calcination and pressing steps. The dry mechanical milling technique enables the formation of well-dispersed and homogeneous materials and realize the desirable reactions. This innovative approach offers several advantages, most notably energy savings. By removing the calcination process, the energy consumption of the synthesis is significantly reduced. Additionally, the absence of pressing the powder into pills simplifies the synthesis procedure and saves time. This novel synthesis method holds promise for improving the efficiency and sustainability of the cathode synthesis process making it more suitable for manufacturing applications, while maintaining or even enhancing the desired properties of the resulting materials.

VII-1   Optimization of Milling Parameters

The main goal herein is to optimize those parameters during mechanochemical ball milling approach, including rotational speed, milling time, the presence or absence of a reverse rotation, the number of rests and its duration, and the weight ratio between balls and materials. By fine-tuning these parameters, it is possible to enhance the efficiency of the synthesis process, improve material properties, and reduce the overall resource expenditure.

To have a good view on the superiority of this novel approach in comparison with conventional methods, the base line materials ($Li_{1.25}Fe_{0.5}Nb_{0.25}O_2$) is first done through the dry milling, in this case the materials are referred to as 0% cation vacancies. The preparation involves adjusting various parameters while keeping some fixed. The weight ratio between the balls and materials is maintained at a fixed value of 23:1, ensuring consistent milling conditions. Additionally, a reverse rotation is always included between the 20 minutes rest, each milling step is kept for 1 hour. The optimization process primarily focuses on the remaining two crucial parameters: rotational speed and milling time. These parameters are systematically varied to determine their impact on the synthesis process, with the aim of achieving optimal material properties and minimizing energy consumption. The following chart (Figure 18) presents the rotational speed and milling time options employed in this thesis during the optimization process.
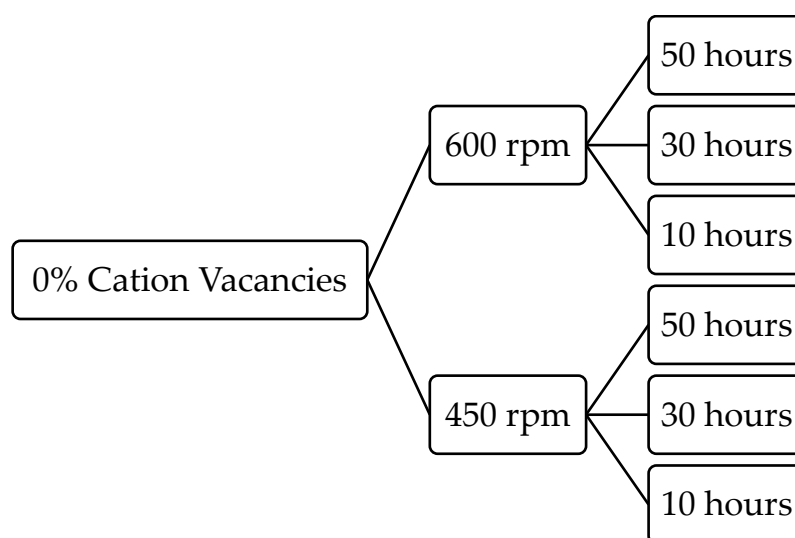
Figure 18 Optimization plan for synthesizing the 0% cation vacancies cathode material via dry milling.

VII-2   Electrochemistry

The charge/discharge curves and corresponding differential (dQ/dV) curves of $Li_{1.25}Fe_{0.5}Nb_{0.25}O_2/C$ (0% cation vacancies) synthesized with different dry milling parameters are shown in Figure 19. Same as the base line materials investigated in the pervious chapter, a voltage range of 1.5 V – 4.8 V is applied.

Figure 19a shows the charge/discharge curve of the material with 0% cation vacancies synthesized at rotational speed of 600 rpm running for a duration of 50 hours. The milling machine stops for a 20-minute rest after every 1 hour of dry milling. The initial observation, when comparing the material with 0% cation vacancies to the baseline material is the difference in charge and discharge specific capacities. The charge specific capacity for the material with 0% cation vacancies is approximately 265 mAh g^{-1}, slightly higher than the baseline material which measures just under 250 mAh g^{-1}. On the other hand, the discharge specific capacity for the material with 0% cation vacancies is around 166 mAh g^{-1}, whereas the baseline material exhibits a higher discharge specific capacity of approximately 200 mAh g^{-1}. The lower discharge capacity observed in the 0%-600 rpm-50 hour material is likely attributed to a reduced involvement of transition metal redox reactions, i.e., the less capacity can be obtained from O1 process (vs. the curve in figure 15b). This could be due to the presence of impure phases within the material. These impurities may interfere with the electrochemical reactions, leading to a decrease in the overall discharge capacity.

The second notable finding regarding the 0%-600 rpm-50 hour material is the presence of a minor discharge plateau (R0) during the initial cycle at a voltage above 3.5 V. This plateau is likely associated with the reduction of Fe^{4+} to Fe^{3+}. In contrast, such a phenomenon is not observed in the baseline material, demonstrating the incompletion of reduction of Fe^{4+} to Fe^{3+} during charge process. This can be a sign for the different atom environment of Fe ions, i.e., stronger Fe-O bounds maybe formed in 0%-600 rpm-50 hour material. Additionally, within the voltage range of 3.5 V to 2.6 V, the 0%-600 rpm-50 hour material exhibits two discharge plateaus (R1 and R2) that correspond to oxygen reduction processes, similar to those observed in the baseline material. Furthermore, below 2.6 V, a discharge plateau (R3) is observed, indicating the reduction of Fe^{3+} to Fe^{2+}. Those R1, R2, and R3 discharge plateaus observed in the 0%-600 rpm-50 hour material are more prominent compared to those in the base line material. This can be attributed to the enhanced Li diffusion facilitated by the smaller particle size achieved through dry milling. The smaller particles provide a larger surface area and shorter diffusion paths for lithium ions, resulting in faster and more efficient Li diffusion within the material. As a result, the redox reactions associated with the discharge plateaus (R1, R2, and R3) exhibit a relatively flat profile.

During the initial charging phase, when the voltage reaches approximately 4.1 V, an observable charge plateau (O1) is detected, indicating the oxidation of Fe^{3+} to Fe^{4+}. Unlike the baseline material, there is no subsequent abnormal reduction process of Fe^{4+} following the oxidation of Fe^{3+} during the first charge. This explains the presence of the discharge plateau (R0) during the initial discharge. During the discharge phase and below 3.5 V, the oxidation state of Fe remains unchanged until the voltage drops to 2.5 V, at which point the reduction process of Fe^{3+} to Fe^{2+} begins. Similar to the baseline material, the stable oxidation state of Fe above 2.5 V during discharge suggests that Fe does not significantly contribute to the high discharge capacity. However, the high discharge capacity is likely derived from the reduction process of oxygen, as indicated by the presence of the R1 and R2 discharge plateaus. Additionally, during the first charge, the oxidation process of oxygen occurs at around 4.4 V, as demonstrated by the second charge plateau (O2). Compared to the base line material, the 0%-600 rpm-50 hour material displays a larger charge plateau (O2), suggesting a higher amount of oxygen redox reactions. This can be attributed to the smaller particle size achieved through dry milling, since oxygen redox reaction is generally in poor kinetics. The enhanced surface area facilitates the relatively low conductivity of the DRX material, resulting in an increased contribution of oxygen redox reactions during the first charge.

In the second charging cycle, the main capacity is contributed by the oxidation of Fe^{2+} to Fe^{3+}. A much shorter plateau (vs. 1st cycle) is observed when the voltage exceeds 3.9 V, thus, the contribution to the total capacity from oxygen redox reaction decreases significantly.

One additional observation in the charge/discharge curve of the 0%-600 rpm-50 hour material is the amplified slope of the transition metal redox region during charge process, which is prominently illustrated in Figure 20. The prolonged slope signifies that with repeated cycling, a greater number of transition metal species (Fe) are being activated and participating in the electrochemical reactions. This suggests an increase in the overall activity and involvement of transition metals within the material as the cycling progresses. However, the heightened slope (indicated by the purple arrow), on the other hand shows the sign of increased inner resistance and over potential inside the cell, which is properly caused by the irreversible change from oxygen reactions.

Overall, the trend indicates that the oxygen redox capacity decreases, but the Fe redox contribution gradually increases with the cycle number.

The detailed electrochemical redox reactions can be further seen through the differential curve of the 0%-600 rpm-50 hour material depicted in Figure 19b. These include the oxidation (O1) and reduction (R3) reactions of Fe, as well as the oxidation (O2) and reduction (R1 and R2) reactions of oxygen. In terms of the first discharge plateau (R0), unlike the baseline material, this dQ/dV graph exhibits a minor indentation above 3.5 V, deviating from a completely flat region. This observation corresponds to the charge/discharge curve where the discharge plateau R0 is observed. Additionally, the dQ/dV curve provides insights into the influence of redox reactions on electrochemical cycling. Similar to the baseline material, the discharge plateaus R1 and R2 display a rapid decrease in their peaks, indicating the irreversible nature of the oxygen reduction reaction. Furthermore, the peak corresponding to the discharge plateau R3, which represents the reduction reaction of Fe, shows a significant decline over cycling, as depicted in Figure 21. This decline highlights the substantial irreversibility of the Fe redox reaction, which explains the pronounced capacity fading observed during cycling, a characteristic that was not observed in the baseline material. Similarly, the oxidation peaks observed in the differential curve show a decreasing trend over cycling, indicating a reduced level of active oxygen participation in the oxidation reactions. This trend reflects the poor reversibility of the oxygen redox process. This poor reversibility is also evident in the charge/discharge curve, where the slope of the oxygen oxidation curve increases with each cycle. This suggests that the oxygen redox reaction becomes more irreversible as the cycling progresses.
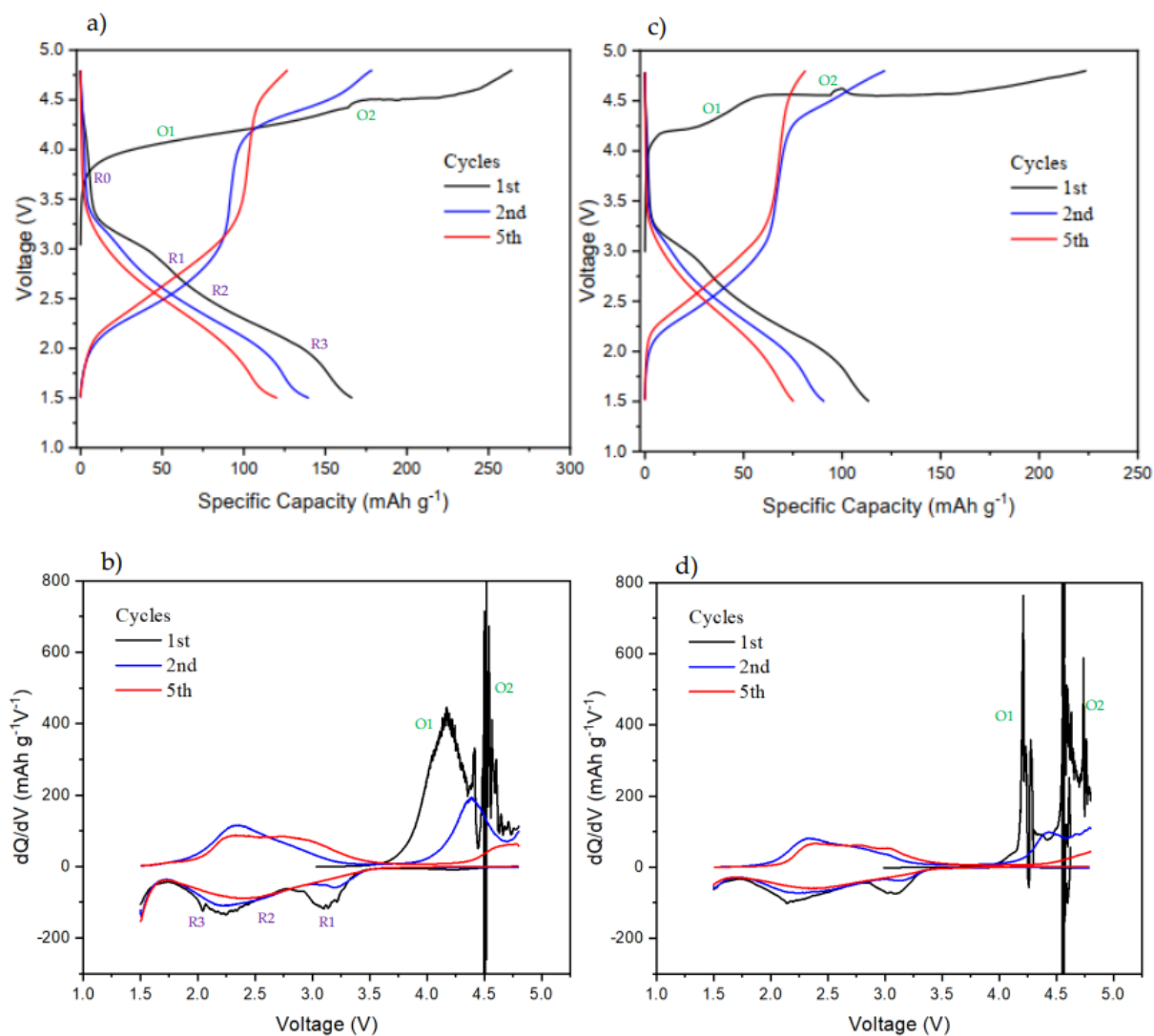
Figure 19 (a) The charge/discharge curve of Li$_{1.25}$Fe$_{0.5}$Nb$_{0.25}$O$_2$/C (0% cation vacancies) with 600 rpm and 50 hour milling parameters. (b) Corresponding differential curve of (a). (c) The charge/discharge curve of Li$_{1.25}$Fe$_{0.5}$Nb$_{0.25}$O$_2$/C (0% cation vacancies) with 600 rpm and 10 hour milling parameters. (d) Corresponding differential curve of (c)
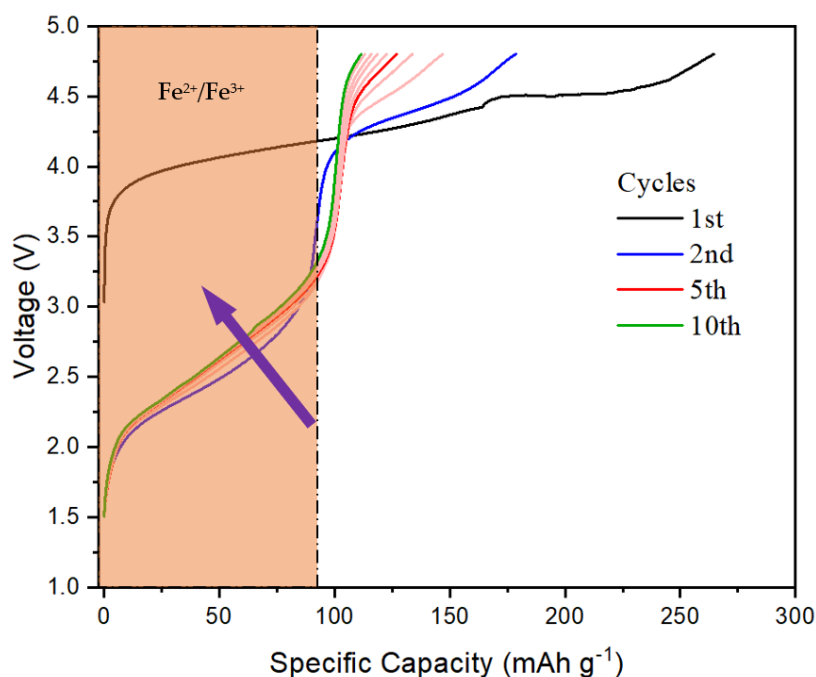
Figure 20 The slope increase of the charging process curve indicates the activation of more transition metal over cycling.
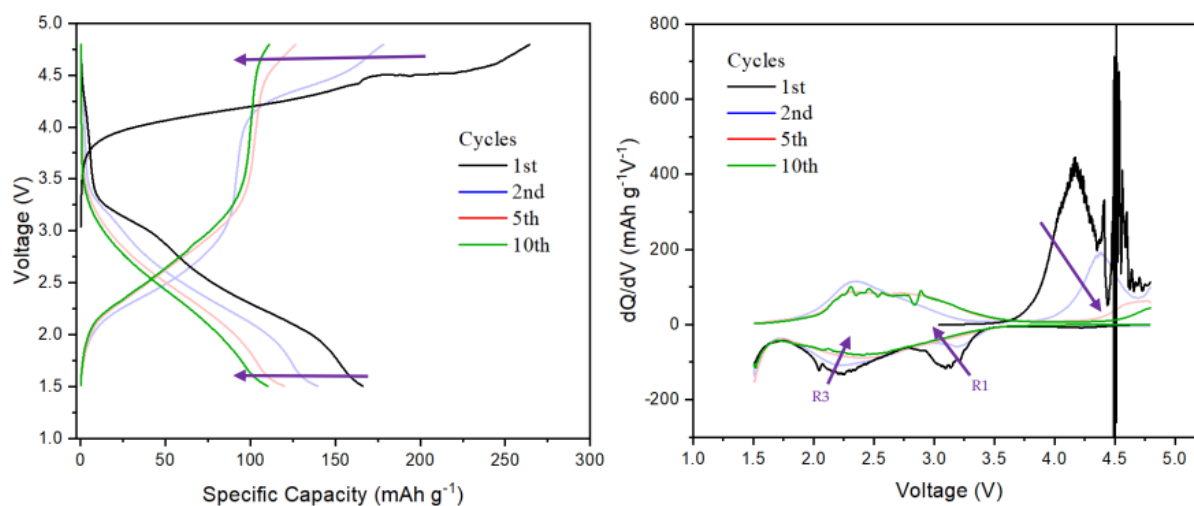
Figure 21 The charge/discharge curve and the corresponding differential curve of the 0%-600 rpm-50 hour material for the 10th cycle.

To understand the influence of milling duration on the material performance, a decrease time of 10 hours is applied for baseline material synthesis, and the obtained sample is named as 0%-600 rpm-10 hour material. This material exhibits a notably lower charge and discharge capacities compared to the 0%-600 rpm-50 hour material,

as depicted in the charge/discharge curve shown in Figure 19c. Furthermore, during the initial charge, the Fe oxidation portion (O1) appears to be shorter, while the oxygen oxidation portion (O2) appears to be relatively longer when compared to the 0%-600 rpm-50 hour material. This can be attributed to the shorter milling time, which has a significant impact on the redox reactions. In this case, the milling time is not sufficient to achieve the disorder rock salt phase necessary for the activation of the transition metal, which can be also discussed later by XRD pattern. On the other hand, oxygen oxidation does not necessarily require the disorder rock salt phase for activation, which explains the longer curve observed during the first charge. Furthermore, Figure 22 illustrates that the contribution of Fe redox reactions in the second charge is lower for the 10-hour material compared to the 50-hour material. This suggests that the 10-hour milling process does not fully activate the Fe redox reactions to the same extent as the 50-hour milling process. The reduced contribution of Fe redox reactions in the 10-hour material further supports the notion that insufficient milling time affects the activation of transition metal redox processes, resulting in diminished electrochemical performance.

The 10-hour milling process also exhibits significant capacity degradation and high irreversibility in the oxygen redox reactions, particularly when compared to the 50-hour milling process. This suggests that a milling duration of 10 hours is insufficient to achieve the desired disorder rock salt phase that effectively activates the transition metal redox reactions. As a result, the 10-hour milling process fails to fully unlock the

electrochemical potential of the material, leading to reduced capacity, high capacity fade and poor reversibility in the oxygen redox reactions.
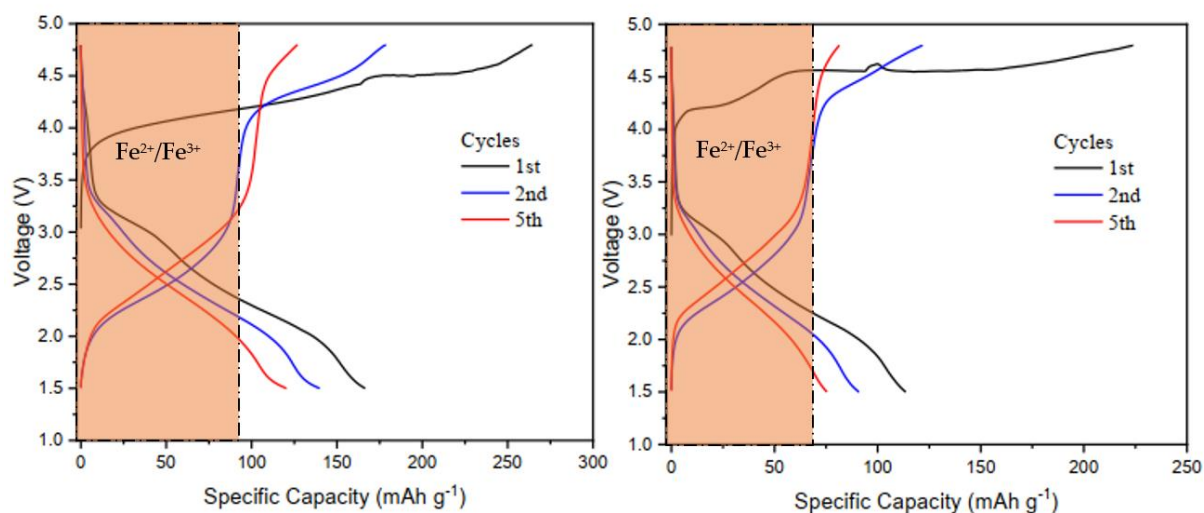
Figure 22 Comparison between the 50 hour milling (left) and the 10 hour milling (right) in terms of the Fe^{2+}/Fe^{3+} oxidation reaction that occurs in the second charge indicated by the shaded area.
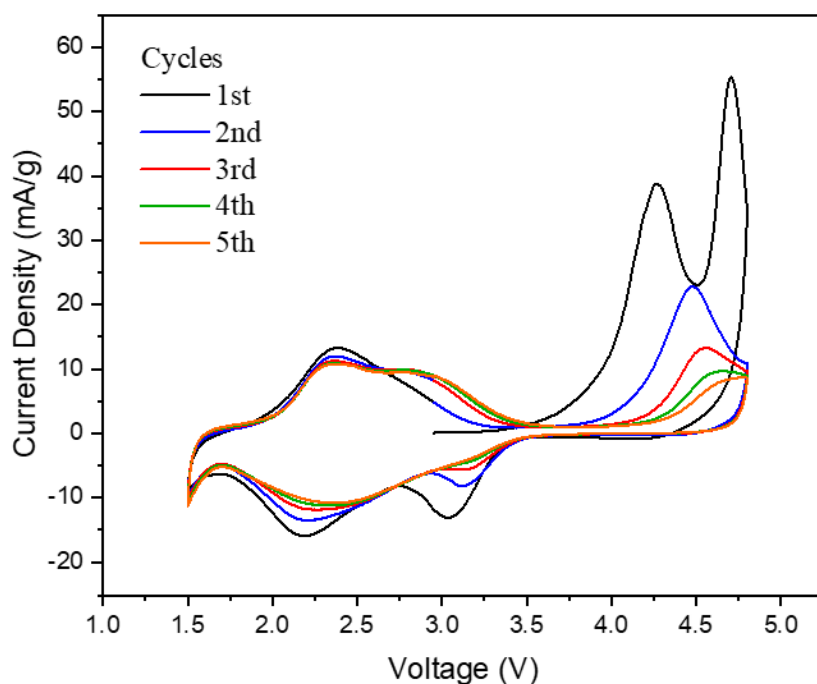
Figure 23 Cyclic voltammogram of 0% cation vacancies-600rpm-50h between 1.5 V and 4.8 V at a scan rate of 5 mV min^{-1}

To assess the impact of oxygen redox on the electrochemical behavior of the cathode material during cycling, cyclic voltammetry (CV) was conducted on the 0%-600 rpm-50 hour material. Figure 23 depicts the cyclic voltammogram recorded at the lower cutoff voltage of 1.5 V and the upper cutoff voltage of 4.8 V, the same as the base line material. The CV curve exhibits an anodic peak (oxidation peak) centered around 4.2 V, indicating the occurrence of an oxidation reaction. Similarly, a cathodic peak (reduction peak) is observed around 2.15 V, representing the corresponding reduction process. Notably, a second anodic peak is present at the upper cutoff voltage, signifying the activation of the oxygen oxidation reaction. Additionally, a second cathodic peak is observed, centered around 3 V, indicating the involvement of the oxygen reduction reaction. The presence of these peaks confirms the participation of oxygen redox reactions in the electrochemical behavior of the 0%-600 rpm-50 hour material.

During extended cycling, the intensity of the oxygen oxidation peak at the upper cutoff voltage and the oxygen reduction peak at 3 V exhibit a notable decrease, indicating the poor reversibility of the oxygen redox reactions, as previously mentioned. Additionally, the oxidation peak corresponding to the transition metal, observed at 4.2 V, continues to shift towards higher voltages and decreases in intensity over cycling. Similarly, the reduction peak associated with the transition metal, located at 2.15 V, also experiences a decrease in intensity. These reductions in peak intensity, accompanied by a decrease in current density, are indicative of hysteresis, voltage fade, and capacity fade occurring in the system.

In contrast to the base line material, the oxygen oxidation peak observed in the cyclic voltammetry (CV) graph for the tested material exhibits comparable prominence to that observed in the corresponding differential curve. This can be attributed to the fast kinetics of the oxygen reaction, which aligns with the fast scan rate employed during the CV test. The enhanced kinetics of the oxygen reaction in this material can be attributed to the smaller particle size achieved through the dry milling process. Consequently, the oxygen peak on the CV graph appears more pronounced in comparison to the base line material.

VII-3   Characterization

In order to characterize the phase of the prepared material, X-ray diffraction (XRD) analysis was conducted, and the results are presented in Figure 24. The XRD patterns of the LFN_0%-50h_600 rpm material show reflections that can be attributed to the *Fm-3m* space group, which is a characteristic of the typical DRX phase. This confirms the successful synthesis of $Li_{1.25}Fe_{0.5}Nb_{0.25}O_2$ DRX material using the dry ball milling method. However, the XRD patterns also indicate poor crystallinity of the target material, as evidenced by the low peak intensities and wide Full Width at Half Maximum (FWHM) values for each main peak. It is possible that the high-energy ball milling approach may have disrupted the crystallinity of the starting reagents or introduced impurities, but no distinct impurity peaks are observed in the XRD pattern. Therefore, while the dry milling method allows the formation of $Li_{1.25}Fe_{0.5}Nb_{0.25}O_2$, the completeness of the reaction cannot be guaranteed. Further characterization techniques for assessing the amorphous nature of the obtained phase would be necessary.

It is worth noting that the XRD pattern of the LFN_0%-50h_450 rpm material also exhibits reflections corresponding to the *Fm-3m* phase, similar to the LFN_0%-50h_600 rpm material. However, there is an additional, less prominent peak observed at 36° 2θ, indicating the presence of an impurity and suggesting the inefficiency of the 450 rpm milling speed. Therefore, the electrochemical characterization primarily focuses on the LFN_0%-50h_600 rpm material due to its better phase purity.

Furthermore, in addition to the low-intensity peaks, some impurities are also detected, particularly in the 10-hour samples. Specifically, in the 0%-450 rpm-10 hour material, two peaks are observed at around 50° and 54° 2θ, and another two peaks are located at 32° and 36° 2θ degrees, which cannot be signed to *Fm-3m* DRX phase corresponding to impure phases. These impure phases can be attributed to other types of Li-rich phase that may be formed instead, one assumption is $LiNbO_3$, since this phase has been reported to be a host of Li ion intercalation because of oxygen redox. However, by increasing the milling speed and, more significantly, prolonging the milling duration, it appears that the formation of $LiNbO_3$ can be prevented, as there are no peaks observed around 50° and 54° 2θ. This indicates a progression towards the desired

phase. In conclusion, increasing the milling time helps to minimize the presence of impure phases.
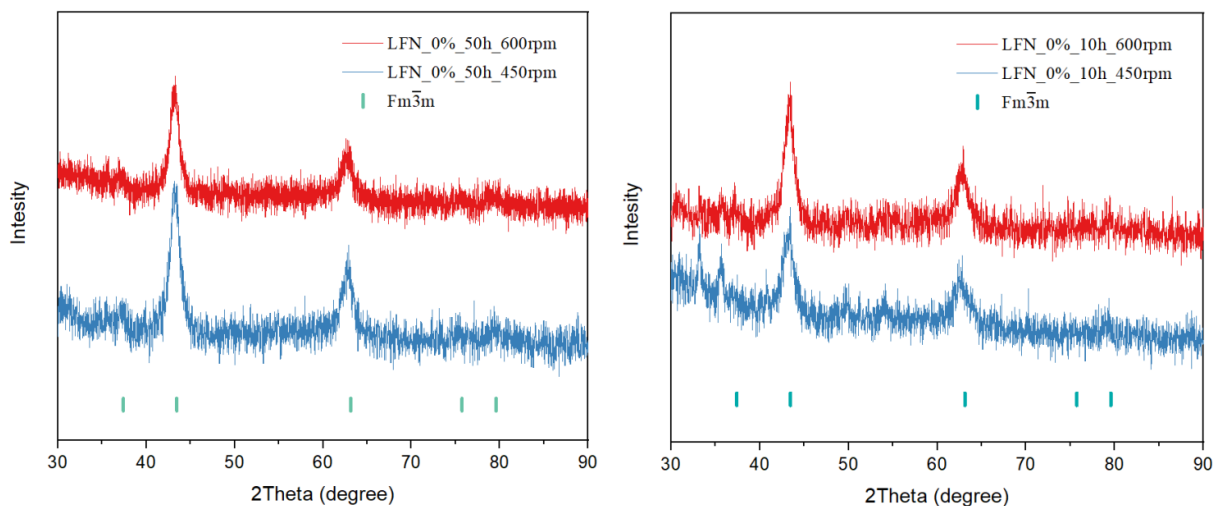
Figure 24 X-ray diffraction (XRD) for the material with 0% cation vacancies.

In addition to the cathode structure and crystallinity, the nanoparticle size and morphology play a significant role in the performance of cathode materials. Scanning electron microscopy (SEM) imaging was performed to investigate these aspects for the baseline material before and after calcination, as well as the material with 0% cation vacancies after 50 hours of dry milling.

Comparing the SEM images of the mixture of starting reagents for baseline material (before calcination) with the 0%-450 rpm-50 hour material, as shown in Figure 25, several observations can be made. In the image of the 0%-450 rpm-50 hour material, there is evidence of better crystallinity, indicating the occurrence of a reaction via dry milling approach. The material appears to have undergone some level of transformation. Conversely, the baseline material before calcination appears as a mixture of unreacted powder particles.

Furthermore, the SEM image of the dry milled material (0%-450 rpm-50 hour) demonstrates certain agglomeration, with the formation of clusters of particles. This suggests the presence of reactions and the development of some interconnected

structures. In contrast, the baseline material before calcination exhibits a more uniform distribution of particles, without notable agglomeration.
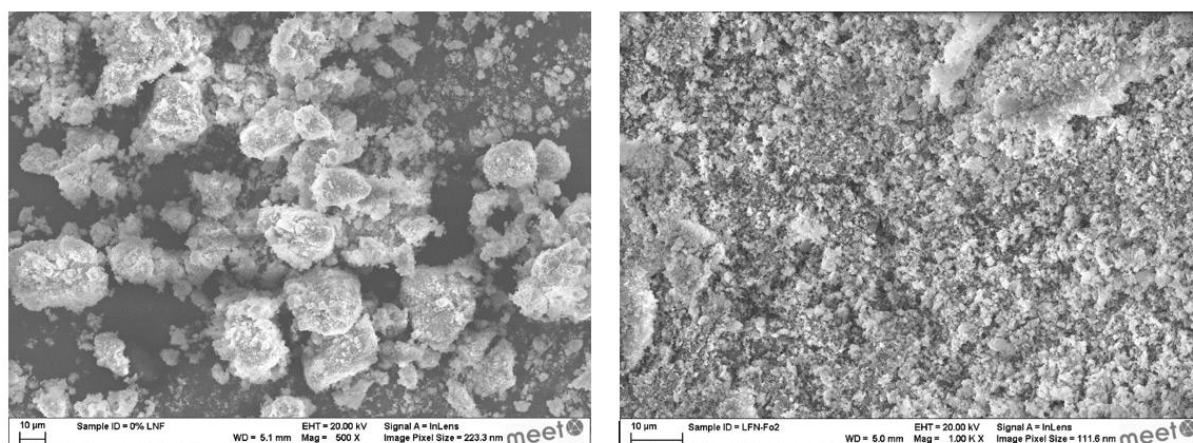
Figure 25 SEM images for the 0%-450 rpm-50 hour material (left) and the mixture of starting regents for base line material before calcination (right)

In Figure 26, a comparison is made between the 0%-450 rpm-50 hour material and the baseline material after calcination. Several observations can be made based on these SEM images:

- Particle Size: The particles in the 0%-450 rpm-50 hour material appears to be much smaller compared to the baseline material after calcination. This reduction in particle size can contribute to improved performance, especially the rate capability, as smaller particles tend to have shortened lithium bulk diffusion path and larger surface area for enhanced reactivity.

- Agglomeration: The dry milling process in the 0%-450 rpm-50 hour material leads to a significant degree of agglomeration, as evident in Figures 26a and 26d. On the other hand, calcination results in a better distribution of particles. The good particle distribution achieved after calcination is favorable for achieving a homogeneous mixing of conductive carbon and active materials during the slurry preparation process. In contrast, the agglomeration of particles in the 0%-450 rpm-50 hour material makes it more challenging to achieve a homogeneous slurry.

To address the effect of particle agglomeration on the homogeneity of the slurry after the ball milling process, further investigation and optimization may be needed.

Finding ways to reduce particle agglomeration can help ensure a more uniform distribution of active materials and improve the homogeneity of the slurry preparation process.
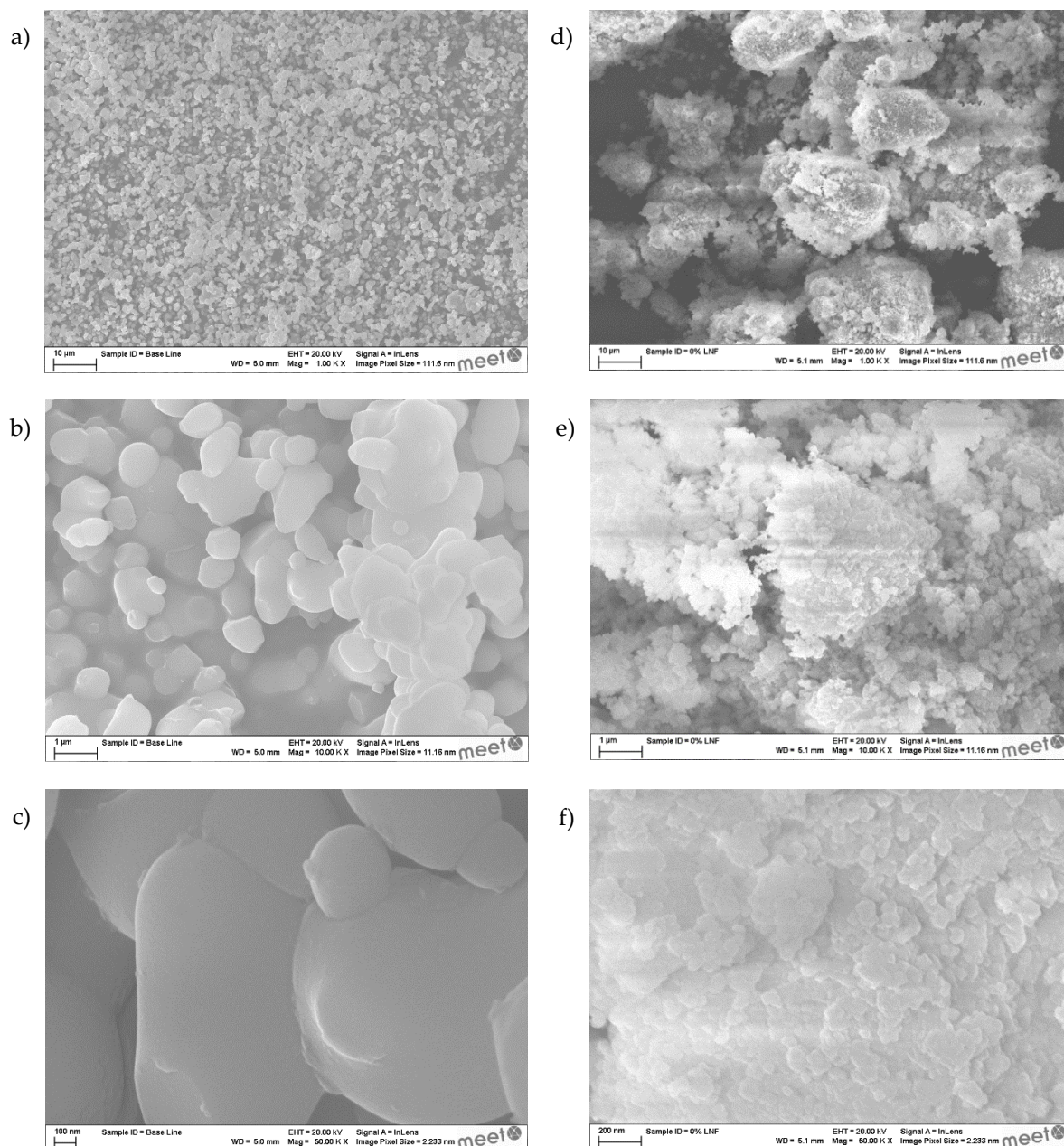
Figure 26 a), b) and c) show the SEM images for the base line material after calcination with different magnification levels, while d), e) and f) show the SEM images for the 0%-450 rpm-50 hour material with different magnification levels.

In addition to SEM images, Energy dispersive X-ray (EDX) element mapping is done to visualize transion metal distribution within the cathode materials. Figure 27 shows the EDX element mapping for the 0%-450 rpm-50 hour material and the base line material after calcination. For both materials, the distribution of the oxygen and transtion metals (Fe and Nb) were found to be homogeneous, indicating the effciency of ball milling in mxing step.
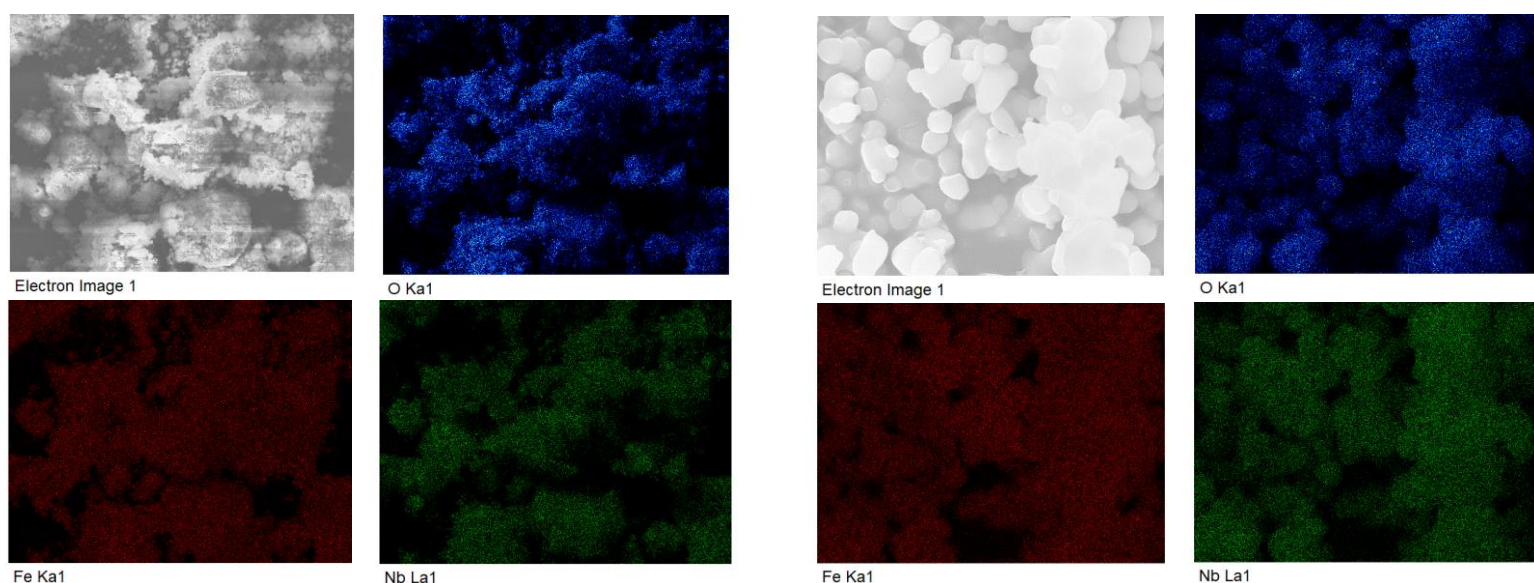
Figure 27 EDX element mapping for the 0%-450 rpm-50 hour material (left) and the base line material after calcination (right)

VIII. STRUCTURAL MODIFICATIONS ON DRX MATERIALS FOR IMPROVED ELECTROCHEMICAL PERFORMANCE

Enhancing the electrochemical performance of cation disorder rock salt cathodes involves various approaches aimed at improving their capacity, cycling stability, and rate capability. There are various methods available accordingly. One strategy is the introduction of chemical doping or substitution of cations to induce disorder in the rock salt structure, which can enhance lithium-ion diffusion and reduce migration

barriers. Another approach is surface modification through coating techniques, such as atomic layer deposition or surface engineering with protective layers, to mitigate side reactions and improve the cathode's stability. Additionally, nano structuring the cathode materials at the atomic or nanoscale can enhance the lithium-ion transport kinetics and shorten diffusion pathways, leading to improved electrochemical performance. Furthermore, optimizing the synthesis process, controlling the particle size, and engineering the cathode-electrolyte interface are crucial aspects that can contribute to enhanced performance in cation disorder rock salt cathodes.

In this chapter, a specific strategy, which involves the creation of cation vacancies using mechanochemical milling as the chosen synthesis strategy will be discussed.

VIII-1   Cation Vacancies

Cation vacancies are intentionally created gaps or vacancies within the crystal lattice of a material by removing specific cations. These vacancies have the potential to offer several benefits to the material's electrochemical performance. First, they can facilitate the movement of lithium ions by creating more accessible pathways, reducing the diffusion distances, and minimizing diffusion barriers. This improved ion transfer can enhance the overall rate capability of the materials. Then, the presence of cation vacancies provides additional sites for lithium-ion intercalation, effectively increasing the material's lithium storage capacity. This chapter aims to investigate whether these anticipated advantages can indeed be achieved through the introduction of cation vacancies in the material.

Cation vacancies are introduced in the material synthesis process by intentionally creating a deficiency of lithium (Li) ions. Thus, during the material design, to maintain chemical balance, the amount of niobium (Nb) is increased to compensate for the reduced Li content while keeping the iron (Fe) content constant. This ensures that the positive and negative ions in the material remain balanced. However, it's important to note that the ratio between cations (Li, Fe, Nb) and anions (O) in the chemical formula does not need to be precisely balanced.

In this experimental work, two materials with different amount of cation vacancies are synthesized and investigated. The first type involves a 2% cation vacancy, resulting in a chemical formula of $Li_{1.2}Fe_{0.5}Nb_{0.26}O_2$ and a cations/anions ratio of 98%. The second type involves a 6% cation vacancy, resulting in a chemical formula of $Li_{1.1}Fe_{0.5}Nb_{0.28}O_2$ and a cations/anions ratio of 94%. These variations in the cation vacancies and cations/anions ratio are tested to explore their effects on the electrochemical performance of the material.

VIII-2   2% Cation Vacancies

To optimize the preparation of the 2% cation vacancies ($Li_{1.2}Fe_{0.5}Nb_{0.26}O_2$) through dry milling, a projected plan is followed similar to the 0% cation vacancies. The optimization process involves selecting the appropriate rotational speed and milling time to achieve the desired cation disorder rock salt phase while minimizing energy consumption.

Figure 28 presents different options for rotational speed and milling time. These options serve as parameters that can be adjusted during the optimization process. By varying the rotational speed and milling time, different conditions are tested to determine the optimal combination that yields the desired cation disorder rock salt phase.
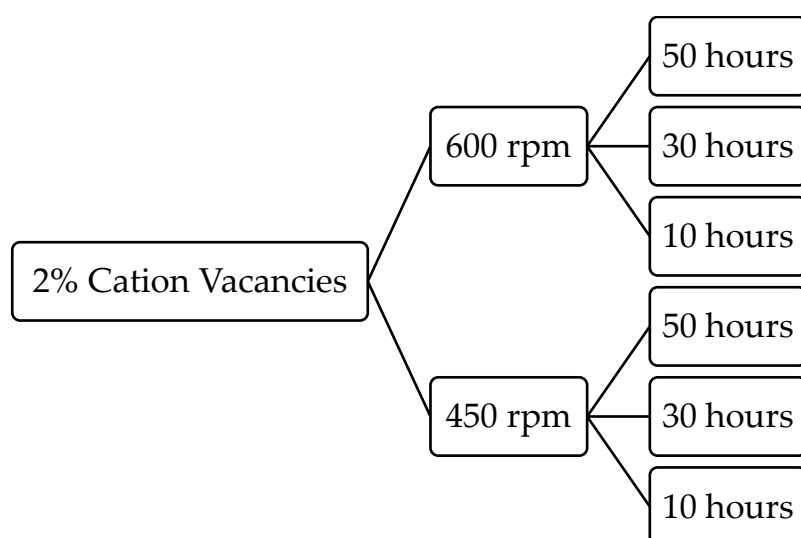
Figure 28 Optimization process plan for synthesizing the 2% cation vacancies cathode material via dry milling.

a) Electrochemistry

Starting with the 2%-600 rpm -50 hour material, its charge/discharge curve, and the corresponding differential (dQ/dV) curve are shown in Figure 29. This material is synthesized at a rotational speed of 600 rpm for 50 hour milling period, employing the same on and off time pattern as the 0%-600 rpm -50 hour material.

Compared to the 0%-600 rpm -50 hour material, the 2%-600 rpm -50 hour material exhibits similar specific charge and discharge capacities, albeit slightly lower. The specific charge capacity for the material with 2% cation vacancies is approximately 255 mAh g^{-1}, while it is 265 mAh g^{-1} for the material with 0% cation vacancies. Similarly, the specific discharge capacity for the material with 2% cation vacancies is around 160 mAh g^{-1}, whereas it is 166 mAh g^{-1} for the material with 0% cation vacancies. The lower specific capacities in the 2% cation vacancies material are likely attributed to the reduced participation of the transition metal redox reaction caused maybe by the presence of impure phases, preventing the desired oxidation of the transition metal during cycling.
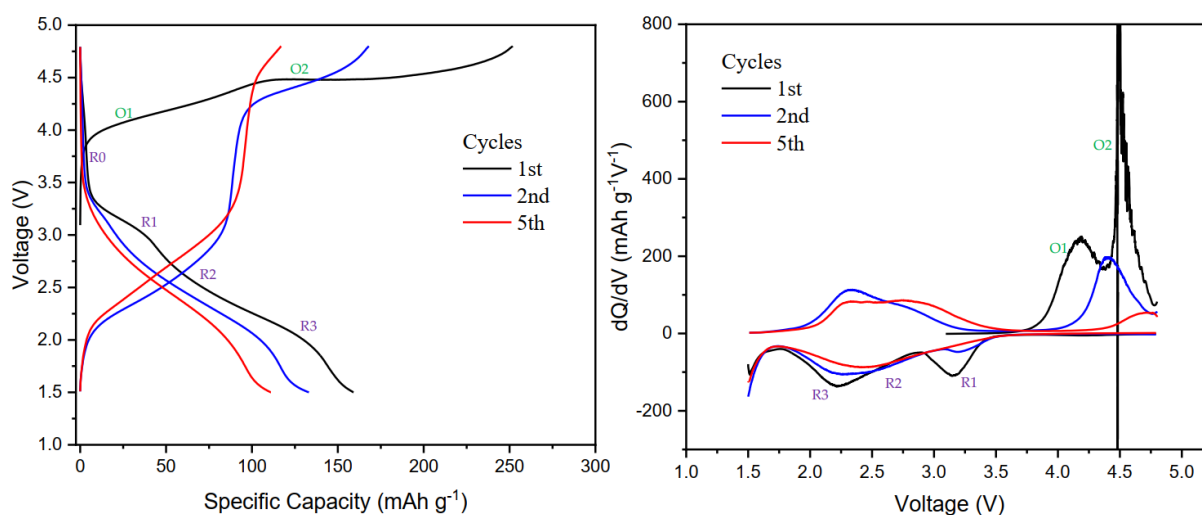
Figure 29 The charge/discharge curve of Li$_{1.2}$Fe$_{0.5}$Nb$_{0.26}$O$_2$/C (2% cation vacancies) with 600 rpm and 50 hour milling parameters and its corresponding differential curve.

Similarly, to the 0%-600 rpm-50 hour material, the 2%-600 rpm-50 hour material also exhibits a small discharge plateau (R0) above 3.5 V in the first discharge cycle,

indicating the reduction of Fe^{4+} to Fe^{3+}. In the voltage range between 3.5 V and 2.6 V, the 2%-600 rpm-50 hour material shows two discharge plateaus (R1 and R2), indicating the occurrence of oxygen reduction processes. Additionally, below 2.6 V, another discharge plateau (R3) is observed, representing the reduction process of Fe^{3+} to Fe^{2+}. Similar to the 0% cation vacancies material, the R1, R2, and R3 plateaus in the 2%-600 rpm-50 hour material are relatively flat in comparison with the materials that obtained via high temperature calcination, which can be attributed to the small particle size achieved through the dry milling process.

During the initial charge of the material with 2% cation vacancies, an oxidation plateau (O1) is observed above 4.1 V, indicating the oxidation of Fe^{3+} to Fe^{4+}. However, this oxidation process of the transition metal is relatively shorter compared to the material with 0% cation vacancies, as depicted in Figure 30. Following this initial oxidation, part of the Fe remains in its oxidized state until the end of the charge process. On the other hand, during discharge, the remained small amount of Fe^{4+} undergoes reduction, as indicated by the R0 plateau, and below 3.5 V, the Fe oxidation state remains unchanged (Fe^{3+}) until the voltage drops to 2.5 V, where the reduction process of Fe^{3+} to Fe^{2+} begins. It is worth noting that the unchanged Fe oxidation state in the voltage range between 3.5 V and 2.6 V during discharge suggests that Fe does not significantly contribute to the high discharge capacity. Instead, the discharge capacity is primarily derived from the reduction process of oxygen, as indicated by the R1 and R2 discharge plateaus.

Furthermore, during the initial charge of the material with 2% cation vacancies, an additional oxidation process occurs at around 4.5 V, corresponding to the oxidation reaction of oxygen (O2). Unlike the shorter oxidation reaction of the transition metal (O1), the oxygen oxidation reaction (O2) is longer in duration, as depicted in Figure 30, especially when compared to the material with 0% cation vacancies. The longer duration of the oxygen oxidation reaction indicates that a higher proportion of oxygen species are actively participating in the redox reaction. This can be attributed to the defections built in the phase crystal via the vacancy design. The metal-oxygen bounds, as a result, become weaker, and activity of oxygen is therefore being promoted.
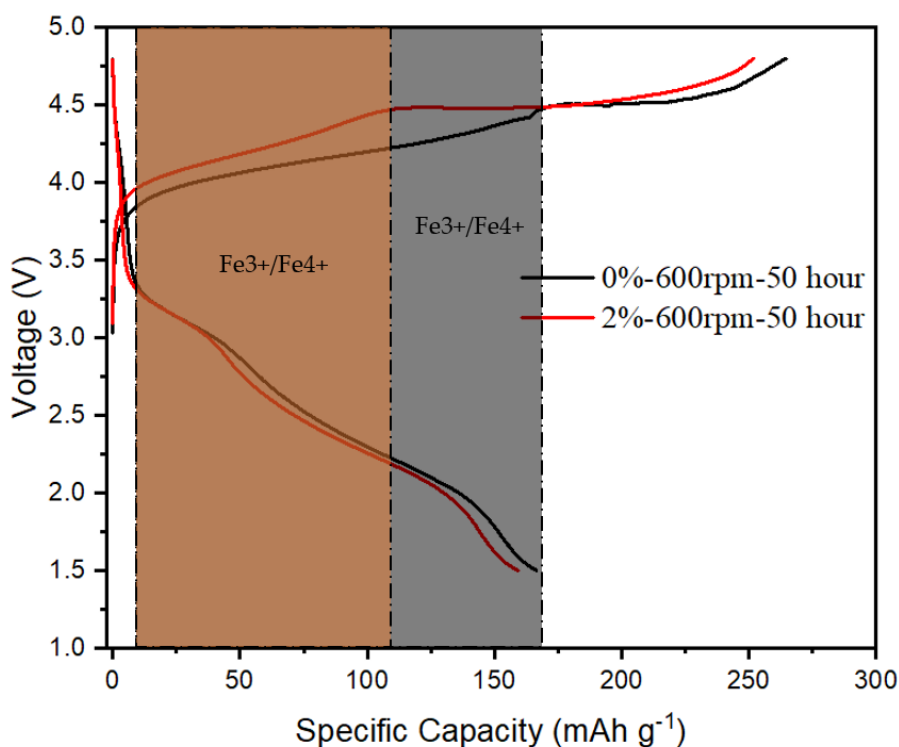
Figure 30 Comparison between the 0% and the 2% cation vacancies in terms of the Fe^{3+}/Fe^{4+} oxidation reaction that occurs in the first charge indicated by the shaded areas.

During the second charge cycle, the reversible oxidation reaction of Fe^{2+} to Fe^{3+} begins at the start of the charge process and continues until the cell voltage reaches approximately 4 V. Beyond this voltage, further charging of the electrode triggers the oxygen oxidation reaction, which persists until reaching the upper cutoff voltage of 4.8 V.

Similar to the 0%-600 rpm-50 hour material, the charge-discharge curve of the material with 2% cation vacancies also exhibits a prolonged slope with the gradually increased voltage in the transition metal redox region over cycling. This observation, as shown in Figure 31, indicates that with repeated cycling, a larger number of transition metal species are participating in the redox reaction. It suggests an enhanced activation of the transition metal redox reactions over cycling even though in combination with slightly increased inner resistance, potentially leading to improved electrochemical performance of the cathode material.
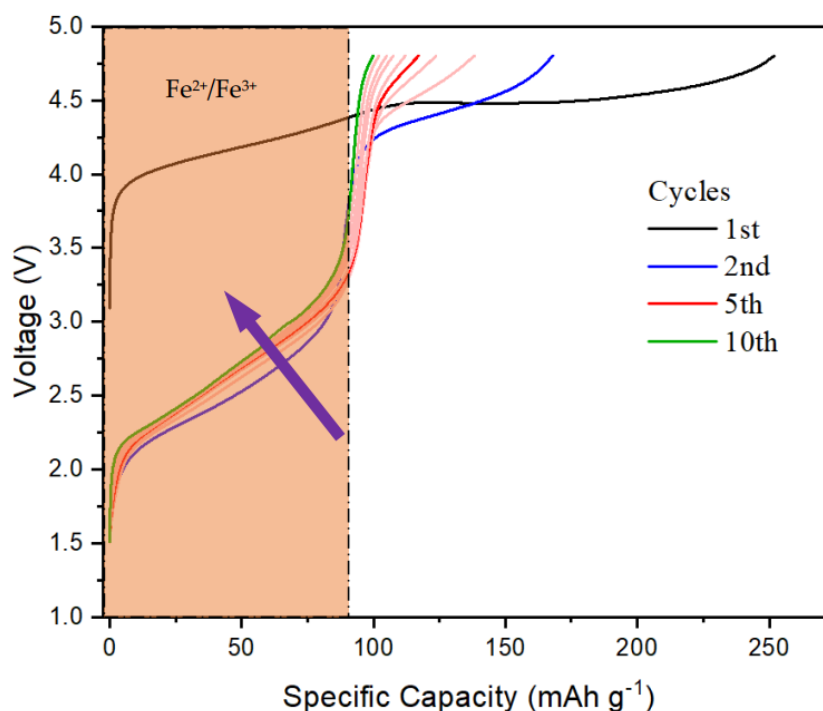
Figure 31 The slope increase of the charging process curve indicates the activation of more transition metal over cycling.

The differential curve of the 2%-600 rpm-50 hour material displayed in Figure 29 provides insights into the oxidation (O1, O2) and reduction (R1, R2, R3) reactions of Fe and oxygen. In the dQ/dV curve, the first discharge cycle exhibits a small dip above 3.5 V, indicating the presence of the R0 discharge plateau. The dQ/dV curve further reveals the influence of redox reactions on the electrochemical performance. The peaks corresponding to R1 and R2 discharge plateaus show a rapid decrease, suggesting the irreversible nature of the oxygen reduction reaction. Similarly, the peak associated with the R3 discharge plateau, representing the reduction reaction of Fe, also exhibits a declining trend over cycling, indicating poor reversibility of the Fe redox reactions. This rapid decrease in peak intensities in the dQ/dV curve, as shown in Figure 32, explains the observed high capacity fading during cycling. Furthermore, the oxidation peaks in the dQ/dV curve also demonstrate a decreasing trend over cycling, indicating a reduced participation of active oxygen in the oxidation reactions and reflecting the poor reversibility of the oxygen redox process. This poor reversibility is also evident in the charge/discharge curve, as indicated by the dramatically shortened slope of the oxygen oxidation region with cycling.
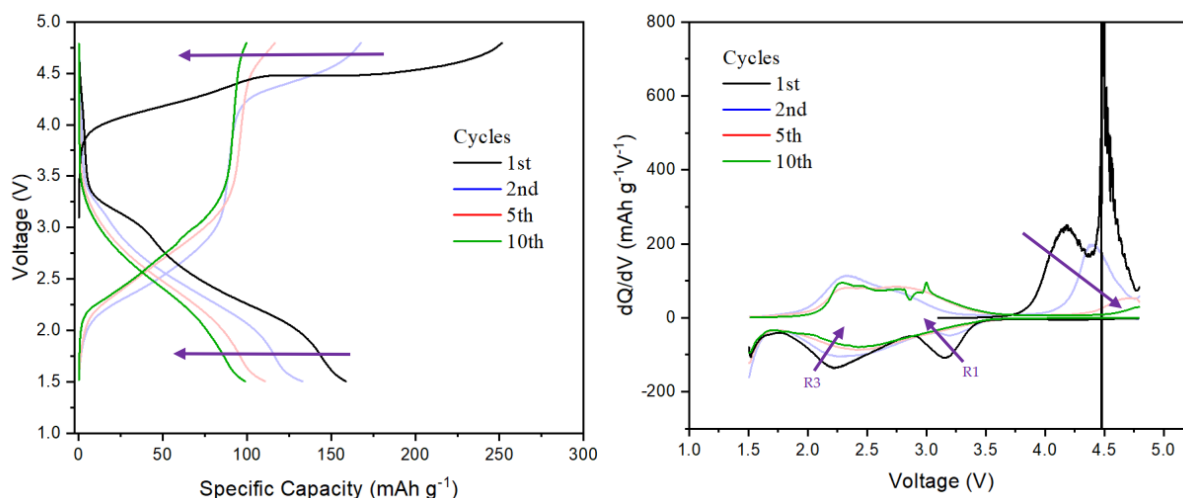
Figure 32 The charge/discharge curve and the corresponding differential curve of the 2%-600 rpm-50 hour material for the 10th cycle.

After noticing the poor performance from the 10 hour material with 0% cation vacancies, short milling time is not the focus in this chapter anymore, i.e., the 50 hour milling time was kept, while changing the rotational speed from 600 rpm to 450 rpm to reveal the influence of the milling speed on materials' electrochemical performance. Figure 33 shows the charge/discharge curve and the corresponding differential (dQ/dV) curve of the 2%-450 rpm-50 hour material.
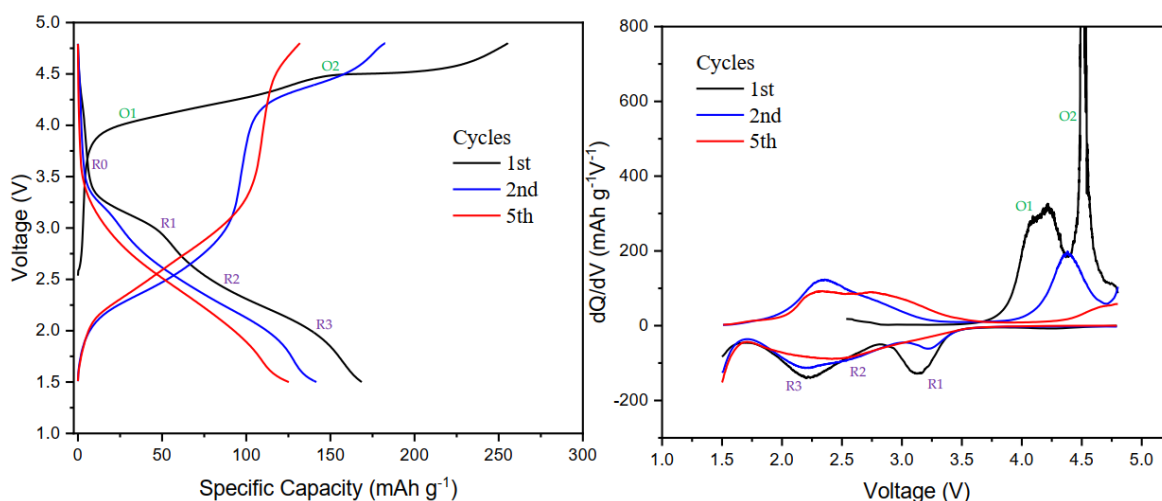
Figure 33 The charge/discharge curve of $Li_{1.2}Fe_{0.5}Nb_{0.26}O_2$/C (2% cation vacancies) with 450 rpm and 50 hour milling parameters and its corresponding differential curve.

Same to all samples prepared via direct dry ball milling, the discharge plateau (R0) is always there in the first cycle indicating the reduction reaction of Fe^{4+} to Fe^{3+} above 3.5

V. Below the 3.5 V until around 2.6 V, R1 and R2 discharge plateaus take place respectively indicating the oxygen reduction reaction. Finally, below 2.6 V, the Fe is reduced again from Fe^{3+} to Fe^{2+} indicated by the final discharge plateau R3. Like the above materials synthesized by dry milling, 2%-450 rpm-50 hour material has a more pronounced R1, R2 and R3 plateaus compared to the base line material and also 0%-600 rpm-50 hour, because of the small size particles obtained through dry milling process and the weaken metal-oxygen bounds leaded by the vacancies.

An interesting finding is that, even though 2%-450 rpm-50 hour material and 2%-600 rpm-50 hour material exhibit very similar charge capacity in the first cycle, the oxidation of the transition metal (Fe^{3+} to Fe^{4+}) occurs at approximately 4.1 V in the 2%-450 rpm-50 hour material is clearly longer, (represented by the charge plateau (O1)), resulting in a higher specific charge capacity, as depicted in figure 34. This suggests that to synthesize the material with 2% cation vacancies, a rotational speed of 450 rpm is high enough to achieve a high proportion of transition metal participating in the redox reaction. Increasing the rotational speed to 600 rpm may end up with the presence of more impure phases and over weaken metal-oxygen bounds that may harm the electrochemical performance of the material.

Following the oxidation of Fe (O1) during the first charge, the oxidation state of part pf Fe remains unchanged until the end of the charge process. In the first discharge, Fe undergoes the first reduction process at R0. Between 3.5 V and 2.6 V, the oxidation state of Fe remains constant before undergoing the second reduction process from Fe^{3+} to Fe^{2+} below 2.6 V. Once again, the negligible change in the oxidation state of Fe between 3.5 V and 2.6 V indicates that the contribution to the discharge capacity primarily arises from the reduction reaction of oxygen rather than Fe.

Furthermore, during the first charge cycle of the 2%-450 rpm-50 hour material, another oxidation process occurs at approximately 4.5 V, representing the oxygen oxidation reaction (O2). The O2 charge plateau is shorter for the 2%-450 rpm material compared to the 2%-600 rpm material, as depicted in Figure 34. Agree with the longer plateau of Fe^{3+} to Fe^{4+}, this indicates that fewer oxygen species participate in the redox reaction due to the lower milling speed of 450 rpm, which results in slightly larger particle sizes

compared to the higher milling speed of 600 rpm which decreases the surface area available for the oxygen reaction.

During the second charge, the reversible oxidation reaction of Fe^{2+} to Fe^{3+} initiates at the beginning of the charge process and persists until the cell voltage reaches approximately 4 V. Subsequently, even though with the significant decrease, as the electrode continues to be charged, the oxygen oxidation reaction is activated and continues until reaching the upper cutoff voltage of 4.8 V.
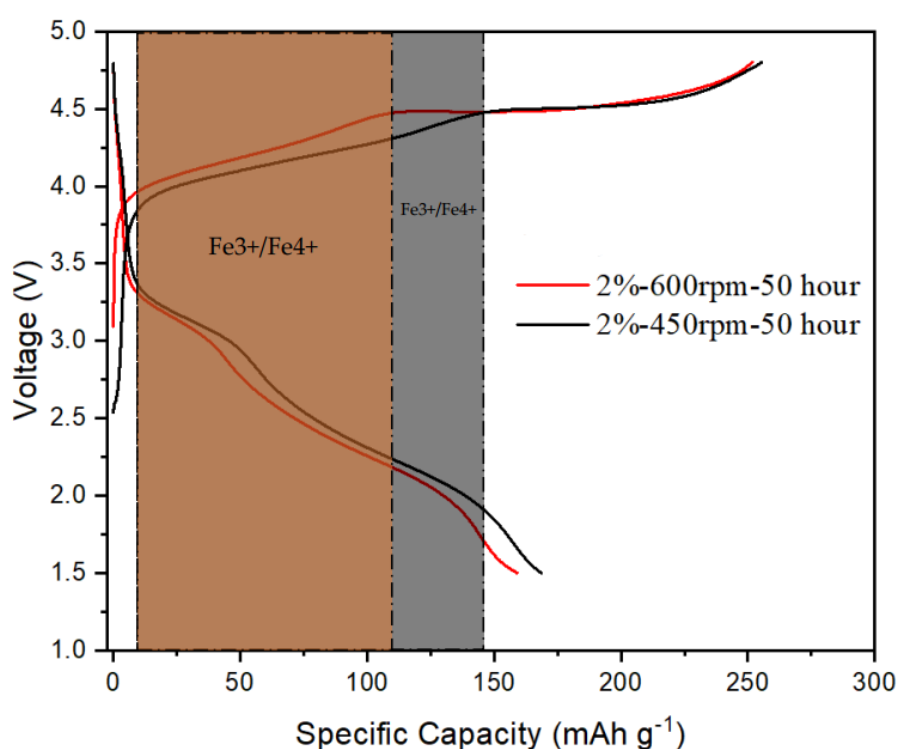
Figure 34 Comparison between the 2%-600rpm and the 2%-450rpm cation vacancies in terms of the Fe^{3+}/Fe^{4+} oxidation reaction that occurs in the first charge indicated by the shaded areas.

The differential curve of the 2%-450 rpm-50 hour material, as shown in Figure 33, provides insights into the oxidation (O1 and O2) and reduction (R1, R2, and R3) reactions of Fe and oxygen. In the dQ/dV curve, the peaks corresponding to the R1 and R2 discharge plateaus demonstrate a rapid decline, indicating the poor reversibility of the oxygen redox process. Similarly, the peak associated with the discharge plateau R3 shows a decreasing trend over cycling, indicating the limited reversibility of the Fe redox reaction. The significant reduction in these peaks, as depicted in Figure 35,

explains the observed capacity fade during cycling. Moreover, the oxidation peaks in the dQ/dV curve also exhibit a decrease in intensity over cycling, indicating the reduced participation of oxygen in the oxidation reaction and reflecting the high irreversibility of the reaction. This behavior is also evident in the charge/discharge curve, where the slope of the oxygen oxidation region increases with cycling.
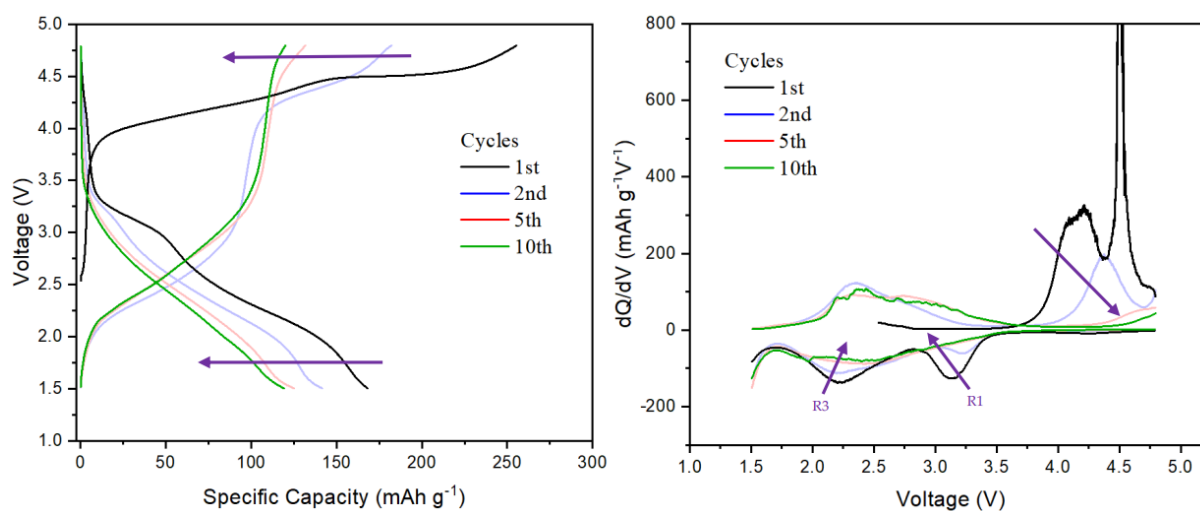
Figure 35 The charge/discharge curve and the corresponding differential curve of the 2%-450 rpm-50 hour material for the 10th cycle.

To investigate the influence of oxygen redox on the electrochemical performance of the cathode material, cyclic voltammetry (CV) was performed on the 2%-450 rpm-50 hour material. Figure 36 shows the cyclic voltammogram obtained within the voltage range of 1.5 V to 4.8 V, which is consistent with the measurement for the base line material. The CV curve exhibits an anodic peak (oxidation peak) at approximately 4.2 V, indicating the occurrence of an oxidation reaction. Similarly, a cathodic peak (reduction peak) is observed around 2.19 V, representing the corresponding reduction process. Importantly, a second anodic peak is observed at the upper cutoff voltage, indicating the activation of the oxygen oxidation reaction. Additionally, a second cathodic peak is observed, centered around 3.1 V, suggesting the involvement of the oxygen reduction reaction. The presence of these peaks confirms the participation of oxygen redox reactions in the electrochemical behavior of the 2%-450 rpm-50 hour material.

During prolonged cycling, the intensity of the oxygen oxidation peak at the upper cutoff voltage and the oxygen reduction peak at 3.1 V exhibit a significant decrease, highlighting the limited reversibility of the oxygen redox reactions, as mentioned earlier. Furthermore, the oxidation peak corresponding to the transition metal, initially observed at 4.2 V, undergoes a gradual shift towards higher voltages and a decrease in intensity over cycling. Similarly, the reduction peak associated with the transition metal, located at 2.19 V, also experiences a decline in intensity. These reductions in peak intensity, accompanied by a decrease in current density, indicate the presence of hysteresis, voltage fade, and capacity fade within the system.
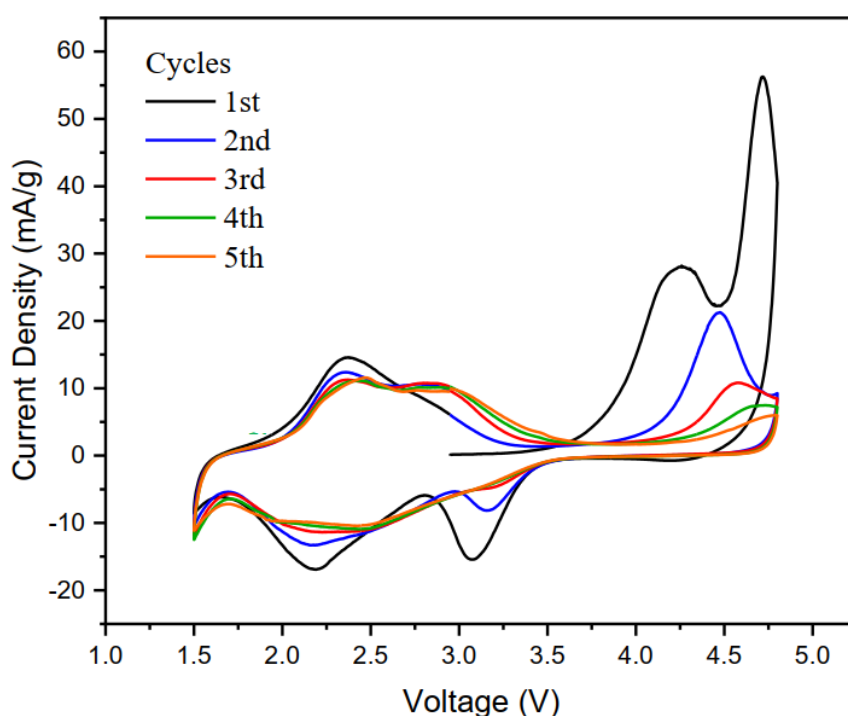
Figure 36 Cyclic voltammogram of 2% cation vacancies-450rpm-50h between 1.5 V and 4.8 V at a scan rate of 5 mV min⁻¹

b) *Characterization*

Figure 37 displays the X-ray diffraction (XRD) patterns for the material with 2% cation vacancies at different milling times and rotational speeds. The pattern of 2%-450 rpm-50 hour material is very much same as the 0%-450 rpm-50 hour material, as displayed in figure 20a, indicating the successful preparation of DRX phase even though may with amorphous impurities. Upon examining the XRD pattern of the 2%-450 rpm-10 hour material, numerous impure phases are observed. Specifically, the first two peaks

at around 33 and 36 degrees correspond to Fe_2O_3, indicating that Fe_2O_3 did not undergo the desired reaction.

Nevertheless, by comparing the prominent peak at approximately 43 degrees in the 2% cation vacancies material, i.e., one of the main reflections in *Fm-3m* DRX phase, with those from impure phases, it is evident that this peak is pronounced, indicating the presence of the desired DRX phase alongside a significant amount of Fe_2O_3. Conversely, the same peak in the material with 0% cation vacancies exhibits a lower intensity, suggesting a higher amount of starting reagents (e.g., Fe_2O_3) participation in the reaction. Additionally, as the milling time increases, similar to the material with 0% cation vacancies, more Fe_2O_3 becomes involved in the reaction, thereby significantly reducing the presence of impure phases. In conclusion, the attempt to introduce vacancies through dry milling synthesis complicates the occurrence of the desired reaction.

Figure 37 X-ray diffraction (XRD) for the material with 2% cation vacancies.

VIII-3   6% Cation Vacancies

To prepare the 6% cation vacancies ($Li_{1.1}Fe_{0.5}Nb_{0.28}O_2$), dry milling was performed using a rotational speed of 600 rpm for a total milling time of 50 hours. During the milling process, the machine was programmed to pause for a 20-minute rest period after every

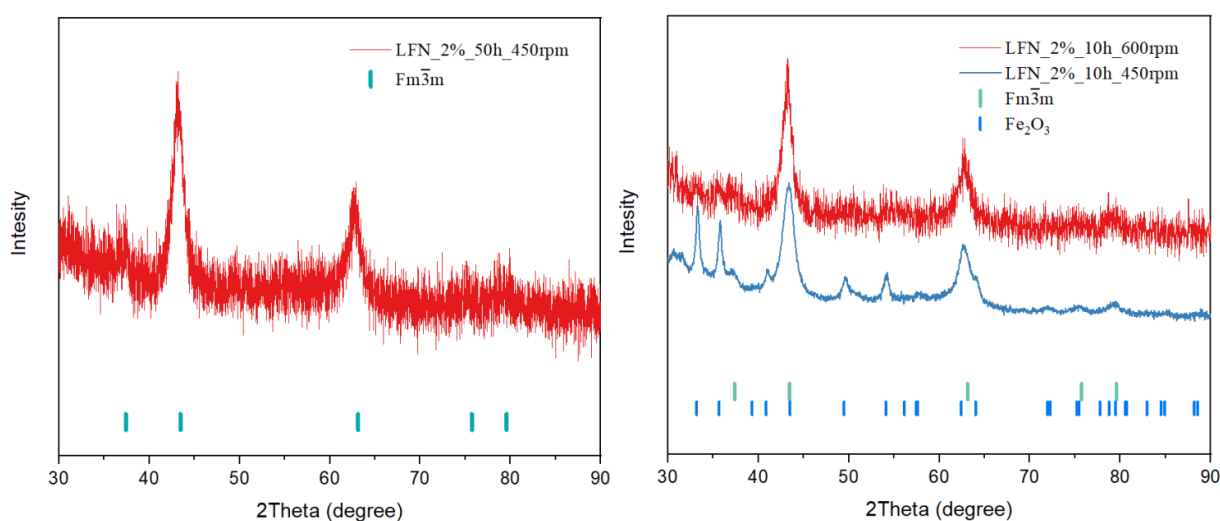1 hour of milling. This intermittent rest period was implemented to prevent excessive heat buildup and ensure optimal milling conditions.

a) *Electrochemistry*

Figure 38 illustrates the charge/discharge curve and the corresponding differential (dQ/dV) curve of the 6%-600 rpm-50 hour material ($Li_{1.1}Fe_{0.5}Nb_{0.28}O_2$), which was cycled between 1.5 V and 4.8 V. Upon analysis of the charge/discharge curve, it can be observed that the charge specific capacity of the material with 6% cation vacancies is 200 mAh g^{-1}, which is the lowest among the tested materials (0% and 2% cation vacancies). Conversely, the discharge specific capacity is approximately 177 mAh g^{-1}, which is the highest among the tested materials. This indicates that the 6%-600 rpm-50 hour material exhibits the closest discharge capacity to that of the base line material and indicates the increased involvement of the transition metal redox reaction.
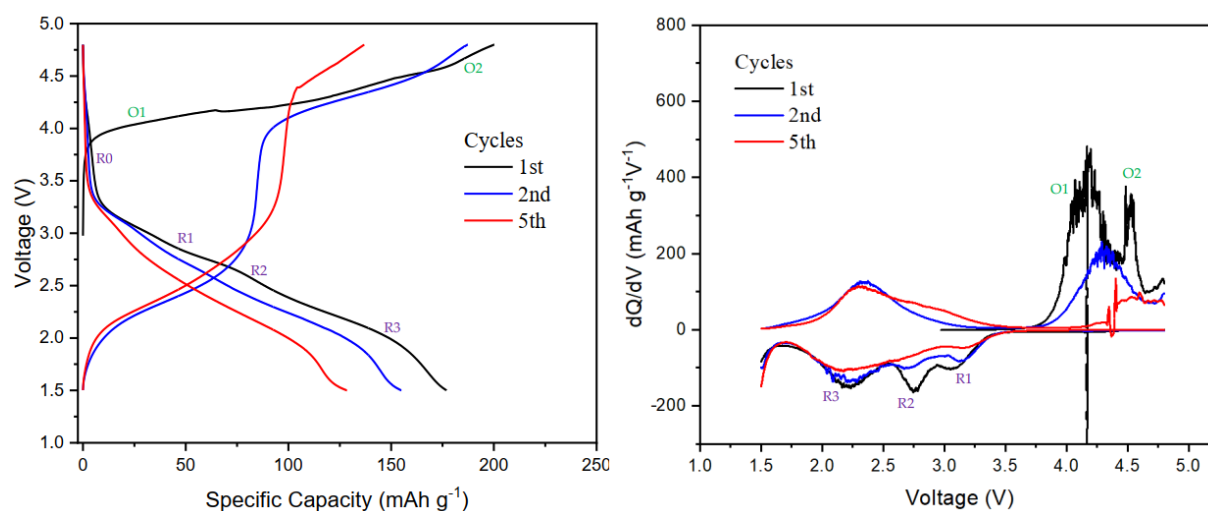
Figure 38 The charge/discharge curve of $Li_{1.1}Fe_{0.5}Nb_{0.28}O_2$/C (6% cation vacancies) with 600 rpm and 50 hour milling parameters and its corresponding differential curve.

Examining the charge/discharge curve of the 6%-600 rpm-50 hour material, several discharge and charge plateaus can be observed, this material, in general, shows similar behavior with other DRX material characterized in this thesis. In the first discharge cycle, a small discharge plateau (R0) is visible above 3.5 V, signifying the reduction process of Fe^{4+} to Fe^{3+}. Furthermore, between the voltage range of 3.5 V and 2.6 V, two discharge plateaus (R1 and R2) are observed, indicating the reduction reaction of

oxygen. Finally, below 2.6 V, the discharge plateau (R3) occurs, representing the second reduction process of Fe^{3+} to Fe^{2+}.

In the material with 6% cation vacancies, the R2 discharge plateau appears more pronounced compared to the R1 discharge plateau, whereas in the materials with 0% and 2% cation vacancies, the R1 plateau is typically more prominent. This difference in the development of the R1 and R2 peaks can be attributed to the specific characteristics of the material with 6% cation vacancies, such as its unique composition and structural properties. The varying prominence of these plateaus suggests differences in the participation and kinetics of oxygen reduction reactions in the different materials, potentially influenced by the presence of more cation vacancies.

During the first charge, the oxidation process of Fe^{3+} to Fe^{4+} occurs at the O1 charge plateau around 4.1 V. Additionally, between 4.5 V and 4.8 V, another oxidation reaction (O2) takes place, which corresponds to the oxygen oxidation reaction. In this voltage range, the oxidation state of Fe remains unchanged. During the first discharge, the oxidation state of Fe remains the same in the voltage range between 3.5 V and 2.6 V. This suggests that the contribution to the discharge capacity primarily comes from the oxygen reduction reaction, rather than the Fe redox process.

In the material with 6% cation vacancies, the first charge plateau (O1) is relatively long compared to the material with 2% cation vacancies, as shown in Figure 39. This suggests that the material with 6% cation vacancies exhibits improved lithium conductivity, which can influence the redox reaction in this voltage range. The specific phase or phases that facilitate lithium diffusion and contribute to the observed conductivity enhancement can be determined through X-ray diffraction (XRD) analysis.

XRD can provide information about the crystal structure and phase composition of the material, allowing for a more comprehensive understanding of the lithium diffusion pathways and the impact of cation vacancies on the electrochemical performance. On the other hand, the second charge plateau (O2) in the material with 6% cation vacancies is very short compared to the materials with 0% and 2% cation vacancies suggesting

that the oxygen oxidation reaction occurring in this voltage range is less prominent or less sustained.
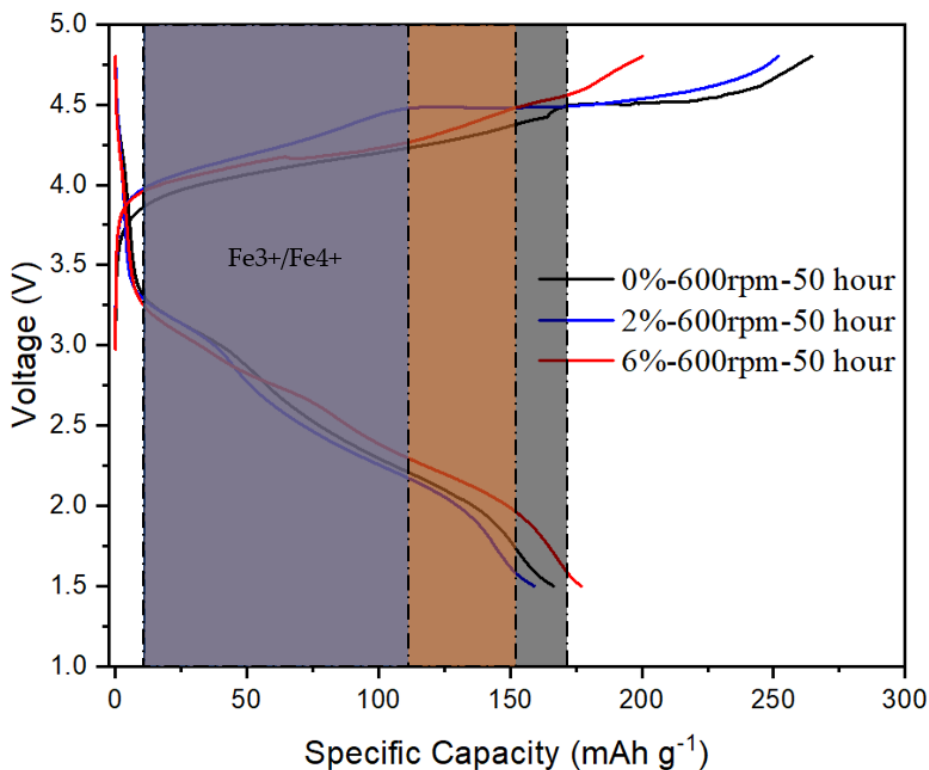
Figure 39 Comparison between the 0%-600rpm, 2%-600rpm and the 6%-600rpm cation vacancies in terms of the Fe^{3+}/Fe^{4+} oxidation reaction that occurs in the first charge indicated by the shaded areas.

During the second charge cycle, the reversible oxidation reaction of Fe^{2+} to Fe^{3+} occurs at the beginning of the charge process and continues until approximately 3.9 V. Beyond 3.9 V, further charging activates the oxygen oxidation reaction, which continues until reaching the upper cutoff voltage of 4.8 V.

The differential curve (dQ/dV) of the 6%-600 rpm-50 hour material depicted in Figure 38, reveals important information about the oxidation (O1, O2) and reduction (R1, R2, R3) reactions of Fe and oxygen. The dQ/dV curve provides insights into the influence of these redox reactions on the electrochemical performance of the material.

In particular, the minor dip observed above 3.5 V in the first discharge cycle indicates the occurrence of the R0 discharge plateau associated with the reduction of Fe^{4+} to Fe^{3+}. The dQ/dV curve also highlights the irreversible nature of the oxygen reduction reaction, as evidenced by the rapid decrease in the peaks corresponding to the R1 and

R2 discharge plateaus. Moreover, the peak related to the R3 discharge plateau, representing the reduction of Fe, shows a declining trend over cycling, indicating poor reversibility of the Fe redox reactions. This reduction in peak intensities, as shown in Figure 40, helps explain the observed high capacity fading during cycling. Additionally, the oxidation peaks in the dQ/dV curve exhibit a decreasing trend over cycling, indicating a reduced participation of active oxygen in the oxidation reactions and reflecting the poor reversibility of the oxygen redox process. This poor reversibility is also evident in the charge/discharge curve, as seen in the increasing slope of the oxygen oxidation region with cycling.
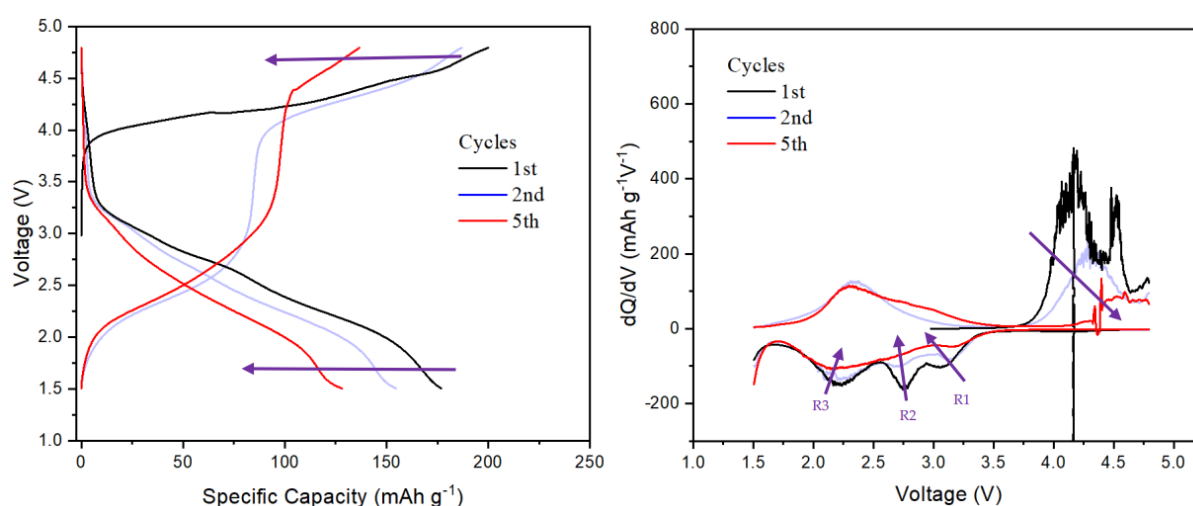
Figure 40 The charge/discharge curve and the corresponding differential curve of the 6%-600 rpm-50 hour material for the 5th cycle.

Cyclic voltammetry (CV) analysis was conducted on the 6%-600 rpm-50 hour material to investigate the impact of oxygen redox on its electrochemical performance. The CV curve, presented in Figure 41 and recorded within the voltage range of 1.5 V to 4.8 V, reveals several key features. An anodic peak (oxidation peak) is observed around 4.2 V, indicating the occurrence of an oxidation reaction. Similarly, a cathodic peak (reduction peak) is identified at approximately 2.2 V, representing the corresponding reduction process. Notably, a second anodic peak is observed at the upper cutoff voltage, indicating the activation of the oxygen oxidation reaction. Additionally, a second cathodic peak is detected, centered around 2.65 V, suggesting the involvement of the oxygen reduction reaction. These peaks confirm the participation of oxygen redox reactions in the electrochemical behavior of the 6%-600 rpm-50 hour material,

although their intensities are relatively low compared to the other materials, as indicated by the small peak at the cutoff voltage.

During cycling, significant decreases in the intensity of the oxygen oxidation peak at the upper cutoff voltage and the oxygen reduction peak at 2.65 V are observed, highlighting the limited reversibility of the oxygen redox reactions, as previously mentioned. Moreover, the oxidation peak associated with the transition metal, initially observed at 4.2 V, gradually shifts towards higher voltages, and experiences a decrease in intensity over cycling. Similarly, the reduction peak related to the transition metal, located at 2.2 V, also exhibits a decline in intensity. These reductions in peak intensity, along with a decrease in current density, indicate the presence of hysteresis, voltage fade, and capacity fade within the system.
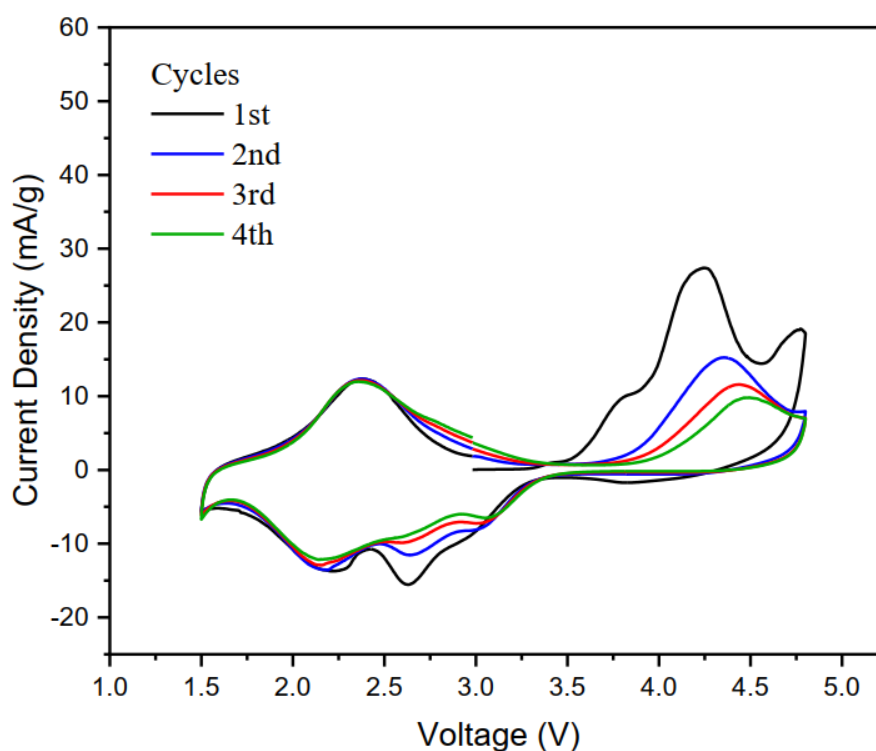
Figure 41 Cyclic voltammogram of 6% cation vacancies-600rpm-50h between 1.5 V and 4.8 V at a scan rate of 5 mV min⁻¹

b) *Characterization*

Even in the extreme conditions of high rotational speed (600 rpm) and long milling time (50 hours), obtaining a super pure phase is still challenging with the 6% cation

vacancies material. The XRD pattern in Figure 42 clearly indicates the presence of impurities, represented by peaks around $52°$ 2θ, which indicate the presence of $LiNbO_3$ (or Li_3NbO_4). In this case, the $LiNbO_3$ is preferred, as less molar of Li salt (vs transition metal) has been introduced during the synthesis, i.e., Li:TM (Fe &Nb) = 1.25:0.75 for 0% cation vacancies sample and 1.1:0.78 for 6% cation vacancies sample. The high amount of Nb in the 6% cation vacancies material makes it difficult to form the desired phase, and instead, Nb tends to react with Li to form $LiNbO_3$, which is a lithium-poor phase compared to the disordered rock salt structure.

Although $LiNbO_3$ exhibits better lithium conductivity, facilitating Li diffusion and explaining the longer plateau of Fe oxidation during the initial charge, it is not electrochemically active as it does not facilitate oxygen redox reactions. Therefore, while $LiNbO_3$ may have some benefits in terms of Li conductivity, it is not desirable from an electrochemical perspective. In conclusion, the process of building vacancies through this method needs further optimization to achieve a purer phase.

Figure 42 X-ray diffraction (XRD) for the material with 2% cation vacancies.

IX. DISCUSSION

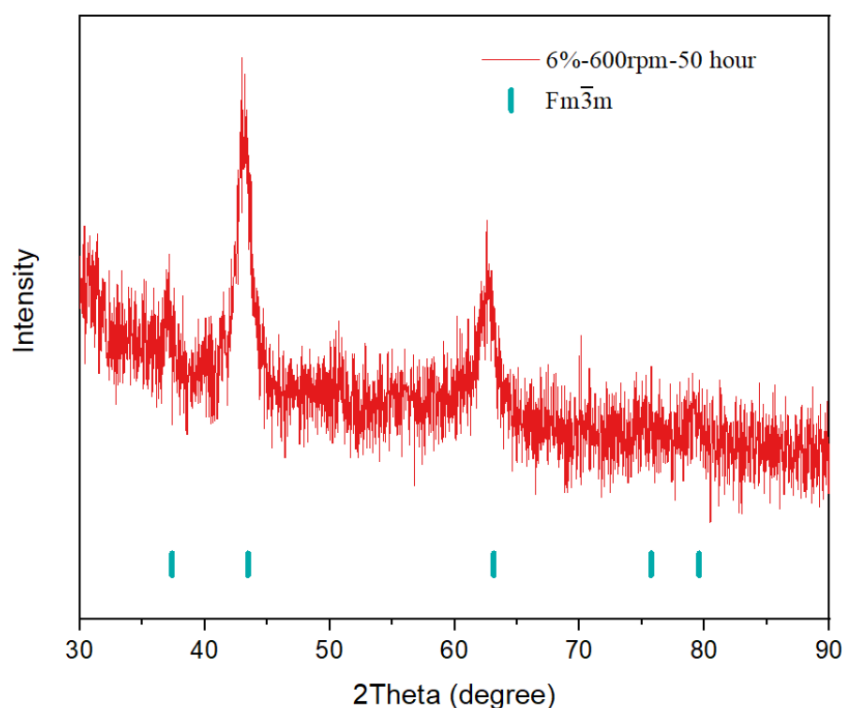Although, the target DRX phase for synthesizing both the base line material and the materials with cation vacancies can be achieved by the mechanochemical ball milling technique, it exhibited poor reproducibility. Despite maintaining a constant material-to-balls ratio, milling time, and rest time for all materials, the dry milling process is subject to uncontrollable factors such as temperature variations influenced by the start time of the milling process, whether it was initiated during the daytime or nighttime. These uncontrolled variables can introduce inconsistencies and affect the reproducibility of the synthesized materials. Furthermore, when sealing the jars in the glovebox to be filled with argon (Ar), it was observed that the internal environment of the glovebox, specifically the levels of oxygen and water, varied from time to time. This inconsistency in the internal environment of the glovebox could potentially affect the quality and integrity of the sealed jars and introduce variations in the experimental conditions.

Initially, during the early stages of the experimental work, the preparation of the slurry showed consistency and resulted in the desired electrode film. However, as the experiment progressed to the material synthesis via mechanochemical ball milling, a notable change was observed in the texture of the slurry, which became excessively sticky compared to the normal consistency. During the electrode preparation, this excessive stickiness posed difficulties in casting the slurry onto the aluminum foil (current collector). Consequently, it became impossible to achieve the intended electrode structure due to the altered slurry texture.

To find out the reason and address the issue of excessive stickiness in the slurry texture and enable the preparation of electrodes for electrochemical analysis, a post-treatment of the prepared materials (suction filtration process) was implemented. This process involved washing the material with distilled water, aiming at tracing and the removal of the Li_2O starting reagent, which does not participate in the desired reactions because of the inconsistent ball milling. If this is the case, a lot of Li_2O that remain in the system without reaction tends to absorb moisture during the slurry preparation, leading to the formation of LiOH. This moisture absorption is detrimental to the PVDF, which is a polymer binder used in the preparation of the slurry. The presence of LiOH can cause

crystallization of the PVDF, resulting in the loss of the elastic ability of polymer and the formation of a sticky texture that hinders proper electrode preparation. Therefore, by performing suction filtration to minimize the presence of LiOH, the slurry's stickiness was mitigated, allowing for successful electrode fabrication and subsequent electrochemical analysis.

Following the washing process, a pH test was performed on the solution collected from the water after using it to wash out the Li_2O from the material. Li_2O is highly soluble in water and reacts vigorously upon contact, resulting in the formation of lithium hydroxide (LiOH). The pH test results corroborate this reaction, as the pH value of the solution showed an increase to approximately 13.2 compared to the initial pH value of around 8.9. This significant rise in pH confirms the presence of LiOH in the collected solution, indicating the existence of Li_2O in the material prepared after dry ball milling, and the successful removal of inactive Li_2O from the material during the washing process.

Figure 43 pH test for the water used before and after washing with suction filtration.

The material obtained after this post-treatment shows no issues anymore in slurry preparation. Figure 44 depicts the charge/discharge curve of the 0%-450 rpm-50 hour material after washing was employed to address the issue of sticky slurry. However, the curve reveals that during the initial charge process, the material exhibits a very low specific charge capacity. This indicates a limited availability of Li ions for the

electrochemical reaction. The majority of Li ions were washed out during the suction filtration process, resulting in a reduced amount of Li participating in the delithiation process (the removal of Li ions). However, the material still contains available sites that can host Li ions, and since the anode (Li metal in this case) contains Li ions, there is an ample supply of Li ions available for the lithiation process (the insertion of Li ions). Therefore, the increased charge capacity observed in the second and subsequent cycles is attributed to Li ions originating from the anode rather than the cathode material. This phenomenon explains the enhanced charge capacity observed in the subsequent cycles of the material with respect to the first cycle.
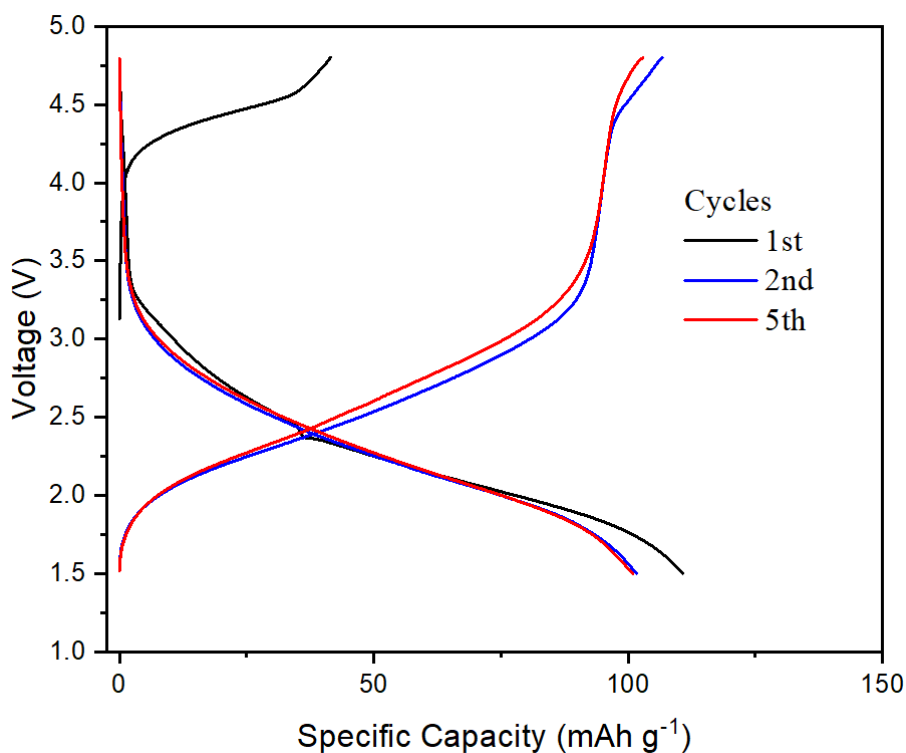
Figure 44 Charge/discharge curve of the 0%-450 rpm-50 hour material after washing with suction filtration.

Unfortunately, though the Li2O has been removed, the discharge capacity does not show improvement, instead, even little. This may be due to the contact with high base solution of the material during the wash step. The structure of DRX phase could be sectored in high alkaline environment, which has been reported for some conventional layered cathode materials (such as high Ni NCM).

Furthermore, as a great amount of Li2O residual in the 0%-450 rpm-50 hour material, certain amount of Fe_2O_3 should be also maintained. This lack of reaction between Li_2O and Fe_2O_3 renders Fe_2O_3 ineffective as a cathode material. Considering the potential application of Fe_2O_3 as an anode material for lithium-ion batteries, the lower cutoff voltage was decreased from 1.5 V to 0.5 V during the electrochemical measurement in order to confirm the presence of Fe_2O_3, the voltage profile of the initial 5 cycles is shown in Figure 45. There are a great number of capacities that can be achieved in the voltage range of 0.5V -1.5 V during discharge, demonstrating the Li intercalation in the Fe2O3 phase. Thus, the incompletion of the reaction for DRX formation is proved in this case, and once again, the poor reproducibility of DRX material synthesis via mechanochemical ball milling method need to be addressed before its scaling up.
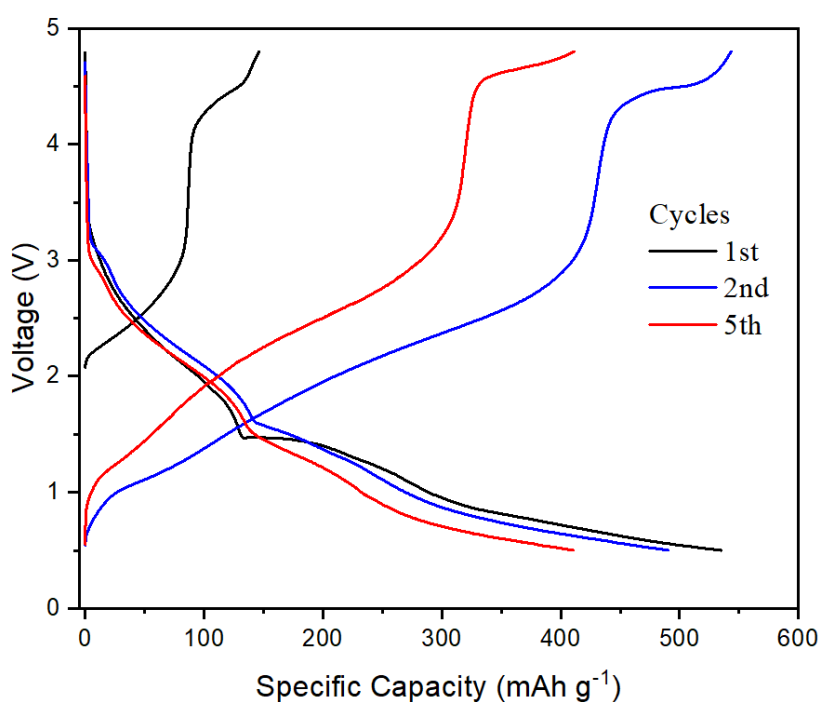

Figure 45 Charge/discharge curve of the 0%-450 rpm-50 hour material after washing with suction filtration with a lower cutoff voltage of 0.5V.

X. CONCLUSION AND PRESPECTIVE

In conclusion, the mechanochemical ball milling process was successfully employed to design and synthesize various cation disordered Li-excess cathode oxides, both with

and without cation vacancies. However, some impurities and poor crystallinity were observed in the synthesized materials. Among the materials synthesized using this technique, the 0%-600 rpm-50 hour material exhibited the highest initial charge capacity of approximately 260 mAh g^{-1}, while the 6%-600 rpm-50 hour material displayed the highest initial discharge capacity of around 177 mAh g^{-1}.

Although the 0%-600 rpm-50 hour and 2%-450 rpm-50 hour materials showed relatively acceptable electrochemical performance with charge/discharge capacities close to the baseline material, they experienced significant capacity fade over cycling. Conversely, the 6%-600 rpm-50 hour material demonstrated an even more substantial decrease in capacity, indicating poor cycling stability. Figure 46 illustrates the charge/discharge curves of all the materials for the 1st, 2nd, and 5th cycles.
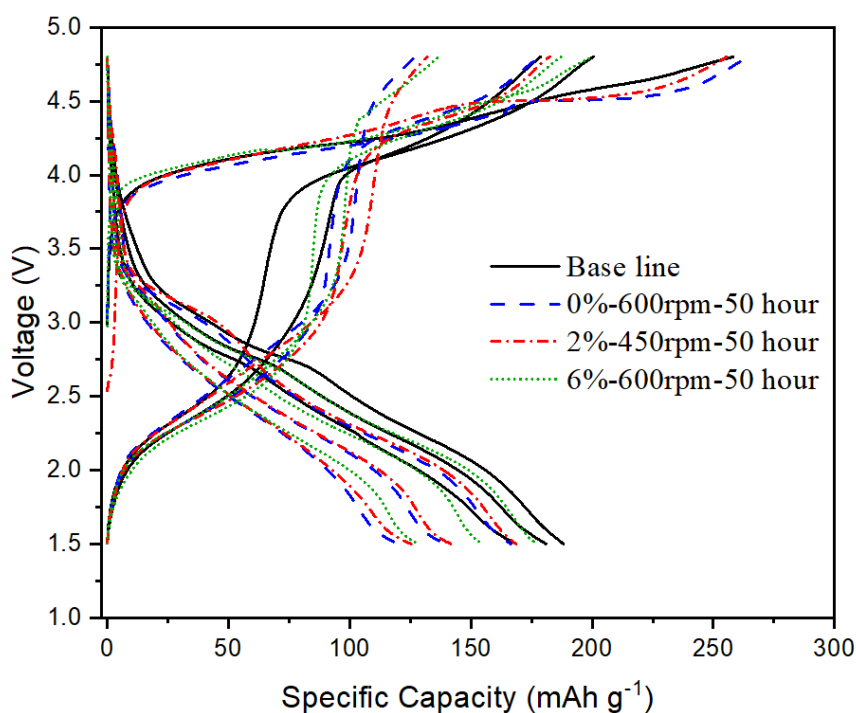
Figure 46 Comparision between the base line material and the other materials synthesized by dry milling only

Comparing one material synthesized by dry milling to the base line material, it is evident from Figure 47 that there is a significant capacity fade observed after cycling for 10 cycles. This substantial decline in capacity indicates that the dry milling synthesis method does not yield the desired pure phase and introduces significant

impurities, which in turn adversely affect the reversibility of the transition metal redox reactions and the cycling stability of the material. Furthermore, while the incorporation of oxygen redox activities can initially increase the cathode capacity, it also contributes to the irreversibility of the redox process, further compromising the cycling stability of the material.

Furthermore, the introduction of cation vacancies through the dry milling technique leads to even poorer crystallinity, resulting in an unstable phase. This instability is a contributing factor to the poor cycling stability observed in the materials with 2% and 6% cation vacancies. As a consequence, these materials exhibit significant capacity fade over cycling, further highlighting the impact of the unstable phase on their electrochemical performance.
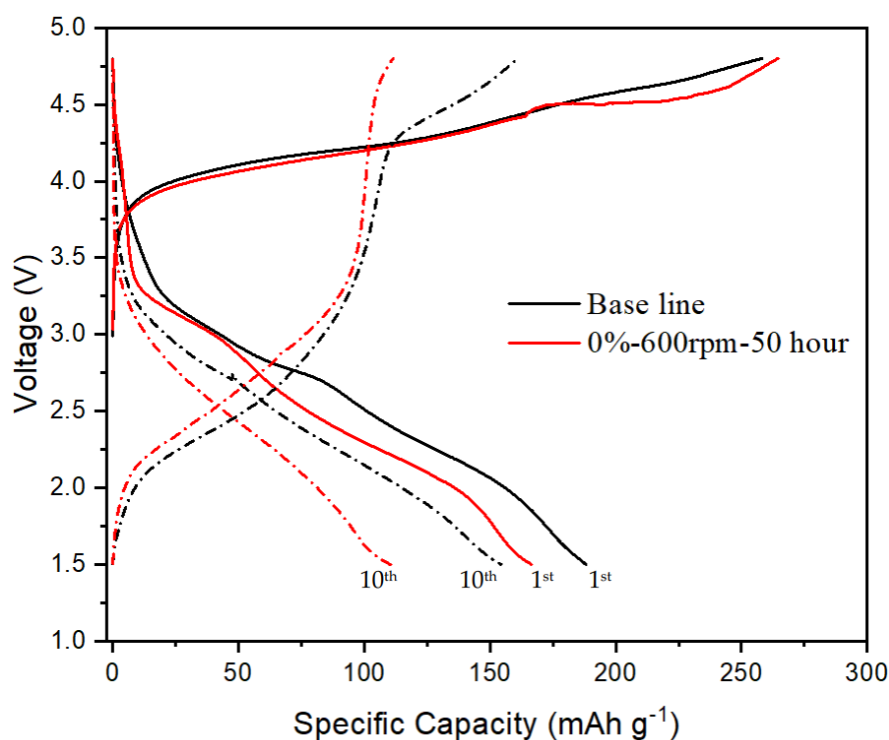
Figure 47 Comparison between the 1st and the 10th cycles for the base line and the 0%-600 rpm-50 hour materials

The findings clearly indicate that the dry milling synthesis technique employed in this study is not optimal and requires further refinement and optimization. It is crucial to address the challenges associated with impurities and phase control to achieve the desired material composition and structure. Moreover, the synthesis process should be optimized to incorporate vacancies in a controlled manner, ensuring an increase in

capacity and improved overall performance. Future research efforts should focus on developing improved synthesis methods that can overcome these limitations and pave the way for the production of high-performance cation disordered Li excess cathode oxides with enhanced capacity and cycling stability.

In future work, it is recommended to conduct the dry milling process in a more controlled environment to ensure consistency in the synthesis of all materials. This could involve better regulation of temperature, humidity, and other parameters to minimize variability. When utilizing Li_2O as the starting reagent, the controlling of humidity should be highlighted in the future. Additionally, during the slurry preparation, using a polytetrafluoroethylene (PTFE) binder or the polymer instead of polyvinylidene fluoride (PVDF) binder can be explored to overcome the issue of stickiness in the slurry texture. PTFE is also a known binder for lithium-ion batteries and can provide better handling and processing characteristics. The compatibility of DRX cathodes and binder materials can be effective to further improve the cell performance. Furthermore, the performance of the cathode material can be enhanced by incorporating fluorine substitution. This approach has shown potential in improving the electrochemical properties of cathode materials, such as higher capacity and enhanced cycling stability. Therefore, exploring fluorine substitution as a means of further optimizing the cathode material is a promising direction for future research and development.

Additionally, in certain cases, even if the ionic conductivity is initially poor due to factors such as low crystallinity, the small particle size achieved through dry milling can facilitate faster Li diffusion. This can potentially enhance the rate capability of the materials, allowing for faster charge and discharge rates. It would be beneficial to test the rate capability of these types of materials in future studies to further understand their performance and potential for high-rate applications.

XI. ACKNOWLEDGEMENT

XII. REFERENCES

[1]   Reddy, M. V., Mauger, A., Julien, C. M., Paolella, A., & Zaghib, K. (2020). Brief history of early lithium-battery development. *Materials*, *13*(8), 1884.

[2]   Scrosati, B. (2011). History of lithium batteries. *Journal of solid state electrochemistry*, *15*(7-8), 1623-1630.

[3]   Brandt, K. (1994). Historical development of secondary lithium batteries. *Solid State Ionics*, *69*(3-4), 173-183.

[4]   Linden, D., & Reddy, T. B. (2002). Handbook of batteries third ed.

[5]   Väyrynen, A., & Salminen, J. (2012). Lithium ion battery production. The Journal of Chemical Thermodynamics, 46, 80-85.

[6]   Letcher, T. (2008). Future energy: Improved, sustainable, and clean options for our planet. Chemistry International--Newsmagazine for IUPAC, 30(2), 20-21.

[7]   Abruña, H. D., Kiya, Y., & Henderson, J. C. (2008). Batteries and electrochemical capacitors. Phys. Today, 61(12), 43-47.

[8]   Xu, J., Dou, S., Liu, H., & Dai, L. (2013). Cathode materials for next generation lithium ion batteries. Nano Energy, 2(4), 439-442.

[9]   Van Schalkwijk, W., & Scrosati, B. (2002). Advances in lithium ion batteries introduction (pp. 1-5). Springer US.

[10]   Scrosati, B., & Garche, J. (2010). Lithium batteries: Status, prospects and future. Journal of power sources, 195(9), 2419-2430.

[11]   Schmuch, R., Wagner, R., Hörpel, G., Placke, T., & Winter, M. (2018). Performance and cost of materials for lithium-based rechargeable automotive batteries. Nature Energy, 3(4), 267-278.

[12]   Dixit, M., Markovsky, B., Schipper, F., Aurbach, D., & Major, D. T. (2017). Origin of structural degradation during cycling and low thermal stability of Ni-rich layered transition metal-based electrode materials. The journal of physical chemistry C, 121(41), 22628-22636.

[13]   Erickson, E. M., Schipper, F., Penki, T. R., Shin, J. Y., Erk, C., Chesneau, F. F., ... & Aurbach, D. (2017). Recent advances and remaining challenges for lithium ion battery cathodes. Journal of The Electrochemical Society, 164(1), A6341.

[14]   Fergus, J. W. (2010). Recent developments in cathode materials for lithium ion batteries. Journal of power sources, 195(4), 939-954.

[15]   Schipper, F., Nayak, P. K., Erickson, E. M., Amalraj, S. F., Srur-Lavi, O., Penki, T. R., ... & Aurbach, D. (2017). Study of cathode materials for lithium-ion batteries: Recent progress and new challenges. Inorganics, 5(2), 32.

[16]   Schipper, F., Erickson, E. M., Erk, C., Shin, J. Y., Chesneau, F. F., & Aurbach, D. (2016). Recent advances and remaining challenges for lithium ion battery cathodes. Journal of The Electrochemical Society, 164(1), A6220.

[17]   Yan, J., Liu, X., & Li, B. (2014). Recent progress in Li-rich layered oxides as cathode materials for Li-ion batteries. Rsc Advances, 4(108), 63268-63284.

[18]   Zuo, W., Luo, M., Liu, X., Wu, J., Liu, H., Li, J., ... & Yang, Y. (2020). Li-rich cathodes for rechargeable Li-based batteries: reaction mechanisms and advanced characterization techniques. Energy & Environmental Science, 13(12), 4450-4497.

[19]   Reed, J., & Ceder, G. (2004). Role of electronic structure in the susceptibility of metastable transition-metal oxide structures to transformation. Chemical reviews, 104(10), 4513-4534.

[20]   Eilers-Rethwisch, M., Winter, M., & Schappacher, F. M. (2018). Synthesis, electrochemical investigation and structural analysis of doped Li [Ni0. 6Mn0. 2Co0. 2-xMx] O2 (x= 0, 0.05; M= Al, Fe, Sn) cathode materials. Journal of power sources, 387, 101-107.

[21]   Yue, L., Ma, C., Yan, S., Wu, Z., Zhao, W., Liu, Q., ... & Sun, X. (2022). Improving the intrinsic electronic conductivity of NiMoO4 anodes by phosphorous doping for high lithium storage. Nano Research, 15(1), 186-194.

[22]   Brinkmann, J. P., Ehteshami-Flammer, N., Luo, M., Leißing, M., Röser, S., Nowak, S., ... & Li, J. (2021). Compatibility of Various Electrolytes with Cation Disordered Rocksalt Cathodes in Lithium Ion Batteries. ACS Applied Energy Materials, 4(10), 10909-10920.

[23]   Yabuuchi, N., Takeuchi, M., Nakayama, M., Shiiba, H., Ogawa, M., Nakayama, K., ... & Komaba, S. (2015). High-capacity electrode materials for rechargeable lithium batteries: Li3NbO4-based system with cation-disordered rocksalt structure. Proceedings of the National Academy of Sciences, 112(25), 7650-7655.

[24]   Obrovac, M. N., Mao, O., & Dahn, J. R. (1998). Structure and electrochemistry of LiMO2 (M= Ti, Mn, Fe, Co, Ni) prepared by mechanochemical synthesis. Solid State Ionics, 112(1-2), 9-19.

[25]   Yabuuchi, N., Takeuchi, M., Nakayama, M., Shiiba, H., Ogawa, M., Nakayama, K., ... & Komaba, S. (2015). High-capacity electrode materials for rechargeable lithium batteries: Li3NbO4-based system with cation-disordered rocksalt structure. Proceedings of the National Academy of Sciences, 112(25), 7650-7655.

[26]   Lee, J., Seo, D. H., Balasubramanian, M., Twu, N., Li, X., & Ceder, G. (2015). A new class of high capacity cation-disordered oxides for rechargeable lithium batteries: Li–Ni–Ti–Mo oxides. Energy & Environmental Science, 8(11), 3255-3265.

[27]   Ji, H., Urban, A., Kitchaev, D. A., Kwon, D. H., Artrith, N., Ophus, C., ... & Ceder, G. (2019). Hidden structural and chemical order controls lithium transport in cation-disordered oxides for rechargeable batteries. Nature communications, 10(1), 592.

[28]   Chen, D., Ahn, J., & Chen, G. (2021). An overview of cation-disordered lithium-excess rocksalt cathodes. ACS Energy Letters, 6(4), 1358-1376.

[29]   Van der Ven, A., & Ceder, G. (2001). Lithium diffusion mechanisms in layered intercalation compounds. Journal of power sources, 97, 529-531.

[30]   Kang, K., Meng, Y. S., Breger, J., Grey, C. P., & Ceder, G. (2006). Electrodes with high power and high capacity for rechargeable lithium batteries. Science, 311(5763), 977-980.

[31]   Urban, A., Lee, J., & Ceder, G. (2014). The configurational space of rocksalt-type oxides for high-capacity lithium battery electrodes. Advanced Energy Materials, 4(13), 1400478.

[32]   Van der Ven, A., & Ceder, G. (2001). Lithium diffusion mechanisms in layered intercalation compounds. Journal of power sources, 97, 529-531.

[33]   Van der Ven, A., Bhattacharya, J., & Belak, A. A. (2013). Understanding Li diffusion in Li-intercalation compounds. Accounts of chemical research, 46(5), 1216-1225.

[34]   Lee, J., Urban, A., Li, X., Su, D., Hautier, G., & Ceder, G. (2014). Unlocking the potential of cation-disordered oxides for rechargeable lithium batteries. science, 343(6170), 519-522.

[35]   Clément, R. J., Lun, Z., & Ceder, G. (2020). Cation-disordered rocksalt transition metal oxides and oxyfluorides for high energy lithium-ion cathodes. Energy & Environmental Science, 13(2), 345-373.

[36]   Kang, K., & Ceder, G. (2006). Factors that affect Li mobility in layered lithium transition metal oxides. Physical Review B, 74(9), 094105.

[37]   Lee, J., Wang, C., Malik, R., Dong, Y., Huang, Y., Seo, D. H., & Li, J. (2021). Determining the Criticality of Li-Excess for Disordered-Rocksalt Li-Ion Battery Cathodes. Advanced Energy Materials, 11(24), 2100204.

[38]   Hatton, P., & Uberuaga, B. P. (2023). Short Range Order in Disordered Spinel and the Impact on Cation Vacancy Transport. Journal of Materials Chemistry A.

[39]   Jones, M. A., Reeves, P. J., Seymour, I. D., Cliffe, M. J., Dutton, S. E., & Grey, C. P. Short-range ordering in battery electrode, the 'cation-disordered'.

[40]   Kan, W. H., Deng, B., Xu, Y., Shukla, A. K., Bo, T., Zhang, S., ... & Chen, G. (2018). Understanding the effect of local short-range ordering on lithium diffusion in Li1. 3Nb0. 3Mn0. 4O2 single-crystal cathode. Chem, 4(9), 2108-2123.

[41]   Clément, R. J., Kitchaev, D., Lee, J., & Ceder, G. (2018). Short-range order and unusual modes of nickel redox in a fluorine-substituted disordered rocksalt oxide lithium-ion cathode. Chemistry of Materials, 30(19), 6945-6956.

[42]   Ji, H., Urban, A., Kitchaev, D. A., Kwon, D. H., Artrith, N., Ophus, C., ... & Ceder, G. (2019). Hidden structural and chemical order controls lithium transport in cation-disordered oxides for rechargeable batteries. Nature communications, 10(1), 592.

[43]   Li, C., Zhang, H. P., Fu, L. J., Liu, H., Wu, Y. P., Rahm, E., ... & Wu, H. Q. (2006). Cathode materials modified by surface coating for lithium ion batteries. Electrochimica Acta, 51(19), 3872-3883.

[44]   Myung, S. T., Amine, K., & Sun, Y. K. (2010). Surface modification of cathode materials from nano-to microscale for rechargeable lithium-ion batteries. Journal of Materials Chemistry, 20(34), 7074-7095.

[45]   Chen, Z., Qin, Y., Amine, K., & Sun, Y. K. (2010). Role of surface coating on cathode materials for lithium-ion batteries. Journal of materials chemistry, 20(36), 7606-7612.

[46]   Li, H., & Zhou, H. (2012). Enhancing the performances of Li-ion batteries by carbon-coating: present and future. Chemical Communications, 48(9), 1201-1217.

[47]   Yaroslavtsev, A. B., & Stenina, I. A. (2020). Carbon coating of electrode materials for lithium-ion batteries. Surface Innovations, 9(2–3), 92-110.

[48]   Zheng, J., Zhang, Y., Hu, T., Lv, T., & Meng, C. (2018). New strategy for the morphology-controlled synthesis of V2O5 microcrystals with enhanced capacitance as battery-type supercapacitor electrodes. Crystal Growth & Design, 18(9), 5365-5376.

[49]   Cook, J. B., Kim, H. S., Lin, T. C., Robbennolt, S., Detsi, E., Dunn, B. S., & Tolbert, S. H. (2017). Tuning porosity and surface area in mesoporous silicon for application in Li-ion battery electrodes. ACS Applied Materials & Interfaces, 9(22), 19063-19073.

[50]   Li, L., Liu, P., Zhu, K., Wang, J., Liu, J., & Qiu, J. (2015). A general and simple method to synthesize well-crystallized nanostructured vanadium oxides for high performance Li-ion batteries. Journal of materials chemistry A, 3(18), 9385-9389.

[51]   Kim, H. S., Cook, J. B., Lin, H., Ko, J. S., Tolbert, S. H., Ozolins, V., & Dunn, B. (2017). Oxygen vacancies enhance pseudocapacitive charge storage properties of MoO3− x. Nature materials, 16(4), 454-460.

[52]   Chu, S., Wang, C., Yang, Y., Wang, Y., & Zou, Z. (2014). Developing high-efficiency π conjugated polymer semiconductor for photocatalytic degradation of dyes under visible light irradiation. RSC advances, 4(100), 57153-57158.

[53]   Shi, J., Zhang, J., Yang, L., Qu, M., Qi, D. C., & Zhang, K. H. (2021). Wide bandgap oxide semiconductors: from materials physics to optoelectronic devices. Advanced Materials, 33(50), 2006230.

[54]   van Bommel, A., & Dahn, J. R. (2010). Kinetics study of the high potential range of lithium-rich transition-metal oxides for lithium-ion batteries by electrochemical methods. Electrochemical and Solid-State Letters, 13(5), A62.

[55]   Li, H., Wang, Z., Chen, L., & Huang, X. (2009). Research on advanced materials for Li-ion batteries. Advanced materials, 21(45), 4593-4607.

[56]   Arico, A. S., Bruce, P., Scrosati, B., Tarascon, J. M., & Van Schalkwijk, W. (2005). Nanostructured materials for advanced energy conversion and storage devices. Nature materials, 4(5), 366-377.

[57]   Guan, C., Liu, J., Wang, Y., Mao, L., Fan, Z., Shen, Z., ... & Wang, J. (2015). Iron oxide-decorated carbon for supercapacitor anodes with ultrahigh energy density and outstanding cycling stability. ACS nano, 9(5), 5198-5207.

[58]   Jung, H. G., Myung, S. T., Yoon, C. S., Son, S. B., Oh, K. H., Amine, K., ... & Sun, Y. K. (2011). Microscale spherical carbon-coated Li 4 Ti 5 O 12 as ultra high power anode material for lithium batteries. Energy & Environmental Science, 4(4), 1345-1351.

[59]   Chen, Z., Augustyn, V., Wen, J., Zhang, Y., Shen, M., Dunn, B., & Lu, Y. (2011). High-performance supercapacitors based on intertwined CNT/V2O5 nanowire nanocomposites. Advanced materials, 23(6), 791-795.

[60]   Abdah, M. A. A. M., Azman, N. H. N., Kulandaivalu, S., & Sulaiman, Y. (2020). Review of the use of transition-metal-oxide and conducting polymer-based fibres for high-performance supercapacitors. Materials & Design, 186, 108199.

[61]   Gao, P., Chen, Z., Gong, Y., Zhang, R., Liu, H., Tang, P., ... & Liu, J. (2020). The role of cation vacancies in electrode materials for enhanced electrochemical energy storage: synthesis, advanced characterization, and fundamentals. Advanced Energy Materials, 10(14), 1903780.

[62]   Zhang, N., Cheng, F., Liu, Y., Zhao, Q., Lei, K., Chen, C., ... & Chen, J. (2016). Cation-deficient spinel ZnMn2O4 cathode in Zn (CF3SO3) 2 electrolyte for rechargeable aqueous Zn-ion battery. Journal of the American Chemical Society, 138(39), 12894-12901.

[63]   Hu, T., Yang, J., & Wang, X. (2017). Carbon vacancies in Ti 2 CT 2 MXenes: defects or a new opportunity?. Physical Chemistry Chemical Physics, 19(47), 31773-31780.

[64]   Zhang, Q., Didier, C., Pang, W. K., Liu, Y., Wang, Z., Li, S., ... & Guo, Z. (2019). Structural insight into layer gliding and lattice distortion in layered manganese oxide electrodes for potassium-ion batteries. Advanced Energy Materials, 9(30), 1900568.

[65]   Ramesh, T. N., & Kamath, P. V. (2008). The effect of stacking faults on the electrochemical performance of nickel hydroxide electrodes. Materials Research Bulletin, 43(11), 2827-2832.

[66]   Wang, R., Chen, X., Huang, Z., Yang, J., Liu, F., Chu, M., ... & Xiao, Y. (2021). Twin boundary defect engineering improves lithium-ion diffusion for fast-charging spinel cathode materials. Nature communications, 12(1), 3085.

[67]   Lun, Z., Ouyang, B., Kwon, D. H., Ha, Y., Foley, E. E., Huang, T. Y., ... & Ceder, G. (2021). Cation-disordered rocksalt-type high-entropy cathodes for Li-ion batteries. Nature materials, 20(2), 214-221.

[68]   Huang, L., Zhong, P., Ha, Y., Cai, Z., Byeon, Y. W., Huang, T. Y., ... & Ceder, G. (2023). Optimizing Li-Excess Cation-Disordered Rocksalt Cathode Design Through Partial Li Deficiency. Advanced Energy Materials, 13(4), 2202345.

[69]   Luo, M., Zheng, S., Wu, J., Zhou, K., Zuo, W., Feng, M., ... & Yang, Y. (2020). Identifying the anionic redox activity in cation-disordered $Li_{1.25}Nb_{0.25}Fe_{0.50}O_2$/C oxide cathodes for Li-ion batteries. Journal of materials chemistry A.